Chemical Science

Accepted Manuscript

This article can be cited before page numbers have been issued, to do this please use: Y. Wang, Y. Xue, C. Hung, K. Huang, B. Jiang, C. Tsai, Y. Huang, H. Chen, S. Yang, S. Chien, C. Chen, P. Chou and Y. Cheng, *Chem. Sci.*, 2025, DOI: 10.1039/D5SC04976H.

ROYAL SOCIETY OF CHEMISTRY

rsc.li/chemical-science

View Article Online
DOI: 10.1039/D5SC04976H

Effect of Halogen/Chalcogen Substitution on the Dielectric Constant of Asymmetric Acceptor Alloys to Improve the Efficiency and Stability of Inverted Organic Photovoltaics

Yan-Bo Wang, Yung-Jing Xue, Chieh-Ming Hung, Kuo-Hsiu Huang, Bing-Huang Jiang, Chia-Lin Tsai, Yu-Chi Huang, Hong-Yi Chen, Shang-Da Yang, Su-Ying Chien, Chih-Ping Chen, Pi-Tai Chou and Yen-Ju Cheng**

Y.-B. Wang, Dr. Y.-J. Xue, Dr. K.-H. Haung, Dr. C.-L. Tsai, Y.-C. Huang, H.-Y. Chen, Prof. Y.-J. Cheng
National Yang Ming Chiao Tung University, Department of Applied Chemistry, 1001 University Road, Hsinchu, 30010, Taiwan.
C.-M. Hung, Prof. P.-T. Chou
National Taiwan University, Department of Chemistry, Center for Emerging Materials and Advanced Devices, No.1, Sec. 4, Roosevelt Road, Taipei 10617, Taiwan
Dr. B.-H. Jiang, Prof. C.-P. Chen
Ming Chi University of Technology, Department of Materials Engineering and Organic Electronics Research Center, New Taipei City 24301, Taiwan
Prof. Shang-Da Yang
National Tsing Hua University, Institute of Photonics Technologies, Hsinchu 300044, Taiwan
Dr. S.-Y. Chien
National Taiwan University, Instrumentation Center, No.1, Sec. 4, Roosevelt Road, Taipei 10617, Taiwan
Prof. Y.-J. Cheng
National Yang Ming Chiao Tung University, Center for Emergent Functional Matter Science, 1001 University Road, Hsinchu, 30010, Taiwan
Email: chop@ntu.edu.tw; yjcheng@nycu.edu.tw

View Article Online
DOI: 10.1039/D5SC04976H

Key words: asymmetric, acceptor alloy, bromination, dielectric constant, inverted, organic solar cells.

Abstract

The dielectric constant (ε_r) of non-fullerene acceptors is a key parameter in organic solar cells, significantly influencing exciton dissociation efficiency and charge recombination dynamics. Substituting bromine, characterized by moderate electronegativity and high polarizability, at the *o*-benzodipyrrole core of acceptors effectively modulates their optical properties, molecular packing, and dielectric constants. The asymmetric monobrominated CBrB-Cl acceptor exhibits a more red-shifted absorption spectrum, enhanced crystallinity, and a higher ε_r of 3.92, contributing to a high efficiency of 17.69% in the inverted PM6:CBrB-Cl device. Further, a selenium-incorporated CB-Se acceptor was selected to form a well-matched dual asymmetric acceptor alloy. The combination of heavy bromine and selenium atoms in the CBrB-Cl:CB-Se alloy increase the ε_r of the PM6:CBrB-Cl:CB-Se blend film to 4.23, which in turn reduces exciton binding energy, promotes efficient charge separation, and suppresses charge recombination, as evidenced by a faster charge separation time (τ_{rise} = 0.39 ps) and a longer charge carrier lifetime (τ_{decay} = 309 ps). The inverted PM6:CBrB-Cl:CB-Se device achieved a high PCE of 18.33%, which is considered to be one of the highest among inverted OPV devices. This work reveals that bromine/selenium substitution enhances the dielectric constant and crystalline packing, thereby advancing molecular design and improving device performance.

1. Introduction

Organic photovoltaics (OPVs) have made significant progress in recent years, largely due to the development of Y6-based non-fullerene acceptors (NFAs).[1] Y6 and its derivatives feature an A-D_NA'$_N$D-A structure, with a central *ortho*-benzodipyrrole (*o*-BDP) core vertically fused to a thiadiazole unit (A′) and a curved C-shaped conformation. Structural optimization of the Y6 backbone has enabled the development of high-performance NFAs,[2-7] achieving power conversion efficiencies (PCEs) over 18% in conventional devices.[6, 7] Further enhancement of PCEs of OPVs is hindered by significant energy losses, primarily stemming from the intrinsically low dielectric constant (ε_r) of organic

View Article Online
DOI: 10.1039/D5SC04976H

semiconductors.[8, 9] The ε_r, defined as the relative permittivity of a material compared to vacuum, reflects its ability to store electric flux. Coulombically bound electron–hole pairs (excitons) are initially generated under photoexcitation. Efficient exciton dissociation into free charge carriers is crucial and is strongly influenced by the exciton binding energy (E_b), which is inversely proportional to the ε_r of the material ($E_b \propto 1/\varepsilon_r$).[10] Inorganic solar cells, such as silicon and gallium arsenide, typically possess high ε_r values of 12,[11, 12] while emerging perovskite materials exhibit even higher values of *ca.* 30,[13] enabling spontaneous exciton dissociation. However, most organic semiconductors exhibit relatively low ε_r values of 3-4,[14] resulting in strong Coulombic attraction and significant non-radiative recombination losses. Halogen engineering of organic semiconductors, particularly through bromine substitution, has emerged as an effective strategy to increase the dielectric constant.[15, 16] Compared to fluorine and chlorine, bromine has lower electronegativity (4.0 for F and 3.2 for Cl vs. 2.8 for Br) and a larger atomic radius (0.071 for F and 0.099 for Cl vs. 0.114 nm for Br), resulting in a more polarizable electron cloud. The high polarizability facilitates stronger intermolecular interactions via improved π/p-orbital overlap, promoting enhanced crystallinity and charge transport.[15-18] More importantly, the polarizability of bromine increases the dielectric constant, thereby lowering exciton binding energy, suppressing charge recombination, and improving charge extraction efficiency.[15-17]

Despite the remarkable success of Y6 derivatives, the synthesis of DA'D cores via Cadogan cyclization under harsh conditions remains a synthetic challenge.[19, 20] Furthermore, introducing halogen atoms into the fully substituted Tz-based $D_NA'_ND$ core is not possible, with substitution only limited to the end groups.[21, 22] To address this challenge, we recently developed a structurally simplified A-D_NB_ND-A-type NFA, CB16,[23] which retains the C-shaped skeleton of Y6 while removing the Tz moiety. CB16 exhibited performance comparable to its Y6-based counterpart, highlighting the critical role of the C-shaped framework in promoting 3D grid-like packing motifs that enable efficient multidirectional electron transport.[23] Further molecular engineering of the CB-series architecture expands the structural scope for developing high-performance A-D-A-type NFAs.[24, 25] The removal of the thiadiazole (Tz) unit from the A-$D_NA'_N$D-A framework exposes two unsubstituted sp²-carbons on

View Article Online
DOI: 10.1039/D5SC04976H

the central benzene core, making halogenation of the o-BDP unit possible and thereby opening up a new arsenal for modulating the properties of C-shaped A-D-A type NFAs.[26, 27] Recently, we reported a central difluorinated A-D_NB_ND-A-type acceptor denoted as CFB.[27] Although CFB exhibits a blue-shifted absorption spectrum due to the reduced electron-donating ability of the *o*-BDP unit, the central fluorine atoms enhance intermolecular interactions, and promote more ordered 3D intermolecular packing, effectively suppressing charge recombination in the PM6:CFB device. Unlike the challenging synthesis of fluorinated *o*-BDP-based cores,[27] the *o*-BDP unit offers an ideal scaffold for high-yield electrophilic aromatic bromination, owing to the *para*-directing activation by nitrogen atoms. Asymmetrizing the central ladder-type π-core of A_1-D_1A'D_2-A_2 NFAs, where either D_1 and D_2 or A_1 and A_2 differ structurally, has been shown to improve OPV performance by optimizing molecular packing and increasing both the dipole moment and dielectric constant.[28-31] Introducing asymmetry into the central *o*-BDP moiety via mono-bromination for improving the dielectric constant without altering the overall molecular geometry of the A-D_NB_ND-A-type structure, represents a promising yet unexplored design strategy.

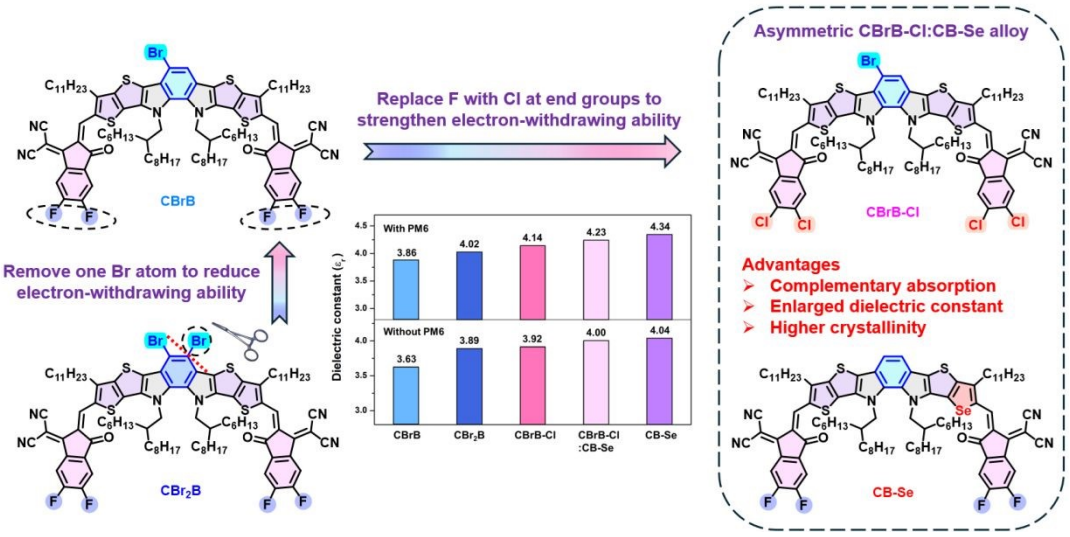

Figure 1. Rational design and chemical structures of halogen-engineered acceptors: CBr_2B, CBrB, and CBrB-Cl; acceptor alloying strategy of CBrB-Cl and CB-Se; and comparison of dielectric constants for the neat acceptor films and their blends with PM6.

View Article Online
DOI: 10.1039/D5SC04976H

In this study, we strategically designed monobrominated and dibrominated D_NB_ND cores, both synthesized efficiently through direct bromination of the formylated D_NB_ND core with high yields. These cores were subsequently condensed with fluorinated indanone (FIC) to produce the symmetric CBr_2B and the asymmetric CBrB. The influence of Br substitution and molecular asymmetry on the electronic, optical and packing properties has been systematically investigated. Bromine's weaker electron-withdrawing nature helps mitigate the issue of blue-shifted absorption in CFB while maintaining favorable interactions with PM6. Furthermore, to enhance intermolecular interactions and intramolecular charge transfer, the FIC end-group in CBrB was replaced with a chlorinated end-group Cl-IC, yielding another asymmetric CBrB-Cl (**Figure 1**). In comparison, CBrB-Cl exhibits a more red-shifted absorption spectrum (λ_{max} = 801 nm), larger dielectric constant of 3.92 (Figure 1) and higher crystallinity. Inverted OPVs generally exhibit superior stability under ambient conditions.[32, 33] However, their efficiencies typically lag behind those of conventional OPVs by 1–2%.[34-36] The processing of CB-series NFAs requires thermal annealing but eliminates the need for additives, making them well-suited for the fabrication of inverted device architectures.[23] Consequently, the inverted binary PM6:CBrB-Cl device delivers the highest PCE of 17.69%. Besides molecular engineering, acceptor alloy, comprising a blend of two distinct NFA materials within the active layer, has emerged as an effective strategy to enhance the efficiency of OPV devices by combining the advantages of each acceptor component.[37, 38] We then introduced another asymmetric CB-Se as a secondary acceptor aiming to further enhance intermolecular interactions via selenium substitution (see Figure 1).[25] The formation of dual asymmetric CBrB-Cl:CB-Se acceptor alloy in the ternary blend capitalizes on the complementary properties of the individual acceptors, including optimized energy level alignment, broadened absorption spectra (λ_{max} of CB-Se at 819 nm), and more ordered molecular packing, resulting in efficient charge transport and minimized energy losses. More importantly, the combination of bromine and selenium atoms in alloy enhances the overall dielectric constant (ε_r = 4.23) of the PM6:CBrB-Cl:CB-Se blend film, which in turn reduces exciton binding energy, promotes efficient charge separation, and suppresses charge recombination, as evidenced by a faster charge separation

View Article Online
DOI: 10.1039/D5SC04976H

time (τ_{rise} = 0.39 ps) and a longer charge carrier lifetime (τ_{decay} = 309 ps) from transient absorption spectroscopy. The inverted device using ternary PM6:CBrB-Cl:CB-Se blend achieved simultaneous enhancements in V_{oc}, J_{sc}, and FF with an impressive PCE of 18.33%. This value represents one of the highest PCEs reported for inverted devices in the literature (see Table S8). It is important to note that the high-performance devices were fabricated by a greener solvent, *o*-xylene, rather than halogenated toxic solvents. The formation of the asymmetric alloy also results in a higher glass transition temperature (T_g) compared to each individual component due to the heteroatom interactions, thereby enhancing the thermal stability of the device.[39, 40]

2. Results and Discussion

2.1 Synthesis

The synthetic routes of CBr_2B, CBrB and CBrB-Cl are depicted in **Scheme 1**. Compound **1** was synthesized following procedures described in the literature.[23] Grignard reaction of compound **1** by isopropyl magnesium chloride lithium chloride complex followed by transmetalation with $ZnCl_2$ resulted in TT-ZnCl, which was further reacted with 2,3-dibromo-1,4-diiodobenzene through Negishi coupling reaction to afford tetrabrominated compound **2** in a yield of 68%.

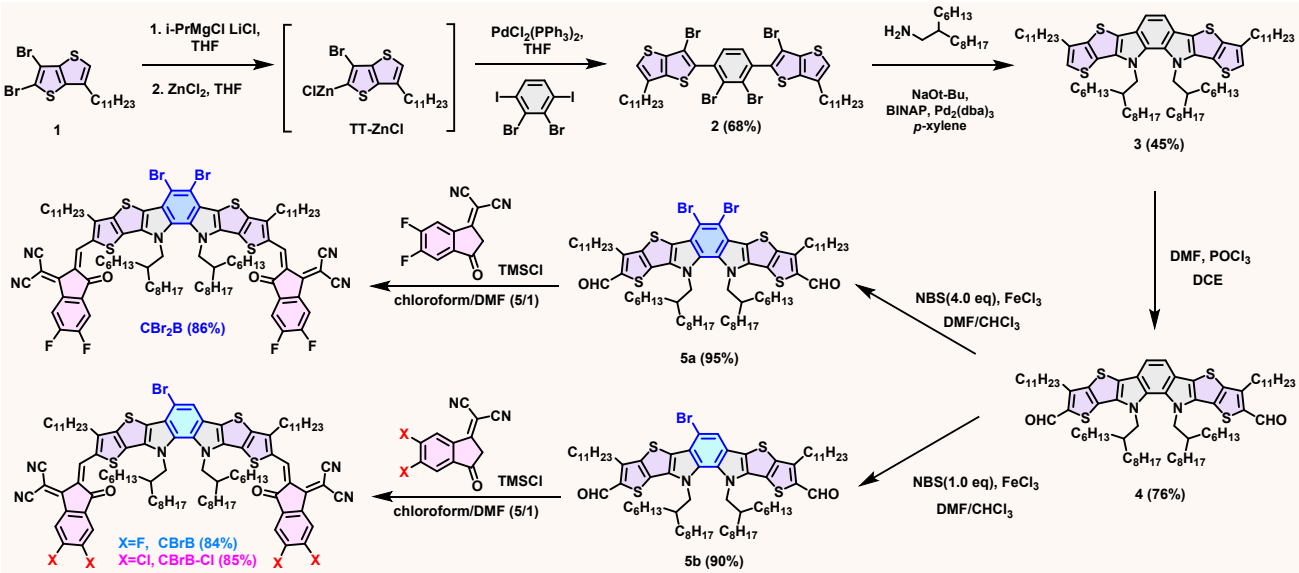

Scheme 1. Synthetic routes for center-brominated CBr_2B, CBrB and CBrB-Cl.

View Article Online
DOI: 10.1039/D5SC04976H

Palladium-catalyzed Buchwald-Hartwig amination of compound **2** with 2-hexyldecyl amine constructed the central *o*-benzodipyrrole moiety in compound **3**. Vilsmeier reaction of compound **3** led to the formation of formylated compound **4**. Direct bromination of compound **4** using four or one equivalent of *N*-bromosuccinimide (NBS) in the presence of ferric chloride efficiently produced the dibrominated compound **5a** and the monobrominated compound **5b**, with yields of 95% and 90%, respectively. Subsequent condensation of **5a** and **5b** with FIC afforded CBr_2B and CBrB, respectively. Additionally, condensation of **5b** with Cl-IC resulted in the asymmetric CBrB-Cl.

2.2 Optical, electrochemical and thermal properties

The absorption spectra are illustrated in **Figure 2a** with the parameters summarized in **Table 1**. Our previous research demonstrated that increasing the electron-withdrawing nature of the heterocycle A' or the substituents on the *o*-BDP moiety led to a blue shift in the absorption spectrum.[27] CBr_2B exhibits a more blue-shifted absorption maximum (λ_{max}) at 710 nm in chloroform compared to Y6-16, which shows λ_{max} at 734 nm, indicating that the stronger electron-withdrawing effect of the two bromine atoms in CBr_2B relative to the thiazole (Tz) unit in Y6-16. It is worth noting that the absorption maximum of CBr_2B is slightly red-shifted compared to its difluorinated analog, CFB (λ_{max} at 704 nm),[27] suggesting that introducing a weaker electron-withdrawing bromine indeed can extend the absorption range of *o*-BDP-based NFAs. Further reducing electron-withdrawing ability by removing one bromine from CBr_2B, forming CBrB, results in a consistent red-shifted λ_{max} to 718 nm. Additionally, replacing FIC with Cl-IC results in the most red-shifted λ_{max} at 734 nm for CBrB-Cl, due to the enhanced intramolecular charge transfer (ICT) effect from the fused backbone to the terminal accepting unit. On the other hand, all three NFAs show a significantly red-shifted absorption maximum when transitioning from chloroform solution to the film state, with $\Delta\lambda$ max values ranging between 60 to 70 nm, indicating strong intermolecular interactions among the three brominated NFAs. To determine HOMO/LUMO energy levels of CBr_2B, CBrB and CBrB-Cl, cyclic voltammetry was employed (Figure S1) with the resulting energy level diagrams illustrated in Figure 2b. CBr_2B exhibits

a deeper HOMO energy level of −5.83 eV and a similar LUMO energy level of −4.01 eV compared to Y6-16, indicating that dibromo atoms may have stronger electron-withdrawing ability over the thiadizole moiety. As a result, the removal of one central bromine elevates both HOMO and LUMO energy levels in CBrB, which is beneficial for increasing the V_{oc} value. CBrB-Cl exhibits deeper HOMO and LUMO energy levels compared to CBrB. However, the difference in LUMO energy between CBrB and CBrB-Cl is larger than that in HOMO energy, resulting in a narrower bandgap for CBrB-Cl, which is advantageous for reducing energy loss.

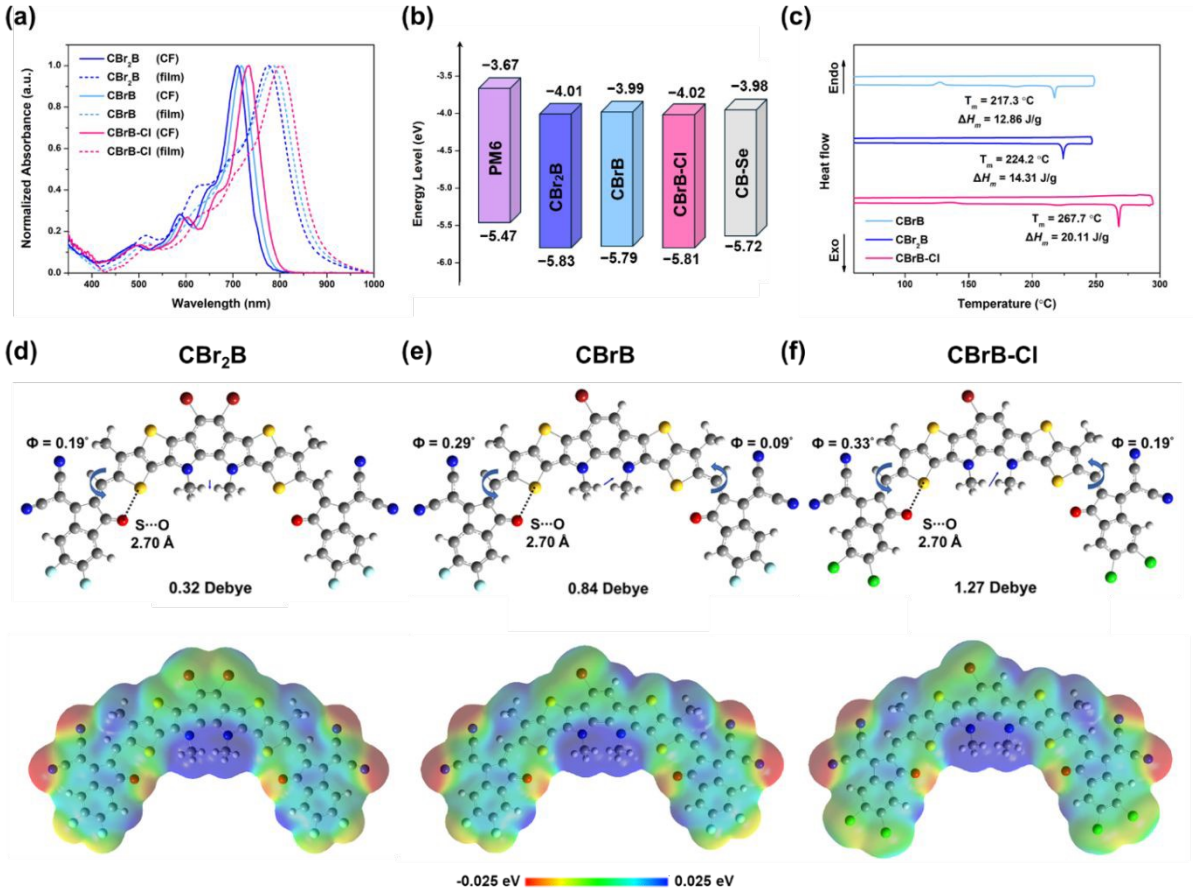

Figure 2. (a) Normalized absorption spectra of CBr_2B, CBrB and CBrB-Cl in chloroform and in film state. (b) Energy levels diagram of PM6, CBr_2B, CBrB, CBrB-Cl and CB-Se obtained from cyclovoltammetry. (c) DSC measurements of CBr_2B, CBrB and CBrB-Cl with a ramping rate of 10 °C /min. Optimized molecular geometries with corresponding dipole moments and electrostatic potential (ESP) distributions for (d) CBr_2B, (e) CBrB, and (f) CBrB-Cl.

View Article Online
DOI: 10.1039/D5SC04976H

To assess the thermal properties, hence the stability of the brominated acceptors, thermogravimetric analysis (TGA) and differential scanning calorimetry (DSC) were conducted (Figure S2 and Figure 2c). All three NFAs exhibit high decomposition temperatures (T_d) around 330 °C, indicating excellent thermal stability. The melting temperatures (T_m) of the NFAs differ significantly. CBrB shows a T_m of 217.3 °C with a fusion enthalpy (ΔH_m) of 12.9 J/g compared to CBr_2B with a higher T_m of 224 °C and a fusion enthalpy of 14.3 J/g, suggesting stronger intermolecular interactions due to the additional bromine atom and the more symmetric structure. For CBrB-Cl, replacing FIC with Cl-IC further enhances intermolecular interactions, resulting in the highest T_m of 267.7 °C and the greatest fusion enthalpy of 20.11 J/g, even surpassing that of the symmetric CBr_2B. The observed trend in T_m and ΔH_m ($CBrB\text{-}Cl > CBr_2B > CBrB$) aligns well with the trend in $\Delta\lambda_{max}$, fully correlating the relationship between molecular structure, intermolecular interactions, and optical properties.

Table 1. Summary of optical and electrochemical properties of CBr_2B, CBrB and CBrB-Cl.

NFA	Extinction coefficient [$x10^5 cm^{-1}M^{-1}$] [a)]	λ_{max}[nm]		$\Delta\lambda$ [nm]	λ_{onset} [nm][b)]	E_g^{opt} [eV][c)]	HOMO [eV][d)]	LUMO [eV][d)]	E_g^{ele} [eV][d)]
		solu	film						
CBr_2B	1.46	710	775	65	860	1.44	−5.83	−4.01	1.82
CBrB	1.68	718	782	64	868	1.43	−5.79	−3.99	1.80
CBrB-Cl	1.72	734	801	67	882	1.41	−5.81	−4.02	1.79

[a)] Calculated at λ_{max} in solution state; [b)]Calculated in the solid state; [c)]$E_g^{opt} = 1240/\lambda_{onset}$; [d)]Determined by cyclic voltammetry.

2.3 Computational frontier molecular orbitals and dielectric constants

Theoretical calculations were performed at the B3LYP/6-311G(d,p) level of theory to obtain the frontier molecular orbitals and electrostatic potential (ESP) diagrams of CBr_2B, CBrB, and CBrB-Cl, as shown in Figure S3 and Figure 2d-f. To simplify the computational process, all side chains were replaced with methyl groups. Compared to CBr_2B, CBrB exhibits elevated LUMO and HOMO energy

View Article Online
DOI: 10.1039/D5SC04976H

levels, indicating that the removal of one bromine atom from the *o*-BDP moiety effectively reduces the central electron-withdrawing effect. This impact is more pronounced on HOMO energy, resulting in a narrower bandgap for CBrB. Additionally, replacing the terminal group FIC with Cl-IC in CBrB-Cl leads to a downshift in both HOMO and LUMO energy levels at −5.93 eV and −3.87 eV, respectively. Notably, the downshift effect is more significant for the LUMO, attributed to the increased electron density localization on the terminal group, which further narrows the bandgap of CBrB-Cl. The influence of bromine atom removal is also evident in the ESP distribution analysis (Figure 2d-f). Asymmetric CBrB and CBrB-Cl display negative ESP on the bromine atoms and positive ESP on the hydrogen atoms of the *o*-BDP moiety, leading to an uneven ESP distribution along the molecular backbone. The molecular dipole moment (μ) of the symmetric CBr_2B was calculated to be 0.32 Debye. In contrast, the asymmetric CBrB, which eliminates one bromine atom, exhibits a significantly higher μ of 0.84 Debye. Substituting the fluorine atoms in CBrB with chlorine to form CBrB-Cl further increases the dipole moment to 1.27 Debye. This substantially larger μ in CBrB-Cl may enhance intermolecular interactions and lead to a different molecular packing pattern compared to the other two NFAs. Another asymmetric NFA, CB-Se, shows a μ of 1.44 Debye, which is comparable to that of CBrB-Cl, and was therefore selected as the acceptor alloy counterpart for CBrB-Cl, which will be discussed in the following sections. The dielectric constants (ε_r) of the three materials were measured by electrochemical impedance spectroscopy to further investigate the effect of heavier heteroatoms. Compared to CBrB, which has a lager dipole moment and a ε_r of 3.63, CBr_2B exhibits an even higher ε_r of 3.89. This result is likely due to the increased polarizability introduced by the additional bromine atom, which is another factor that would affect the value of ε_r. Similarly, CBrB-Cl shows an even higher ε_r of 3.92, which may be attributed to the larger dipole moment of the C–Cl bond. The CB-Se containing a more polarizable selenium atom shows the highest ε_r of 4.04. Adding CB-Se into CBrB-Cl with a ratio of 1:3 also enhances the ε_r to 4.00. The increased ε_r values could contribute to a reduction in exciton binding energy, thereby facilitating exciton dissociation and enhancing charge transport dynamics.[8-10]

View Article Online
DOI: 10.1039/D5SC04976H

2.4 Molecular packing in single crystals

To investigate the influence of di- and mono-bromination in the *o*-BDP core on molecular packing behavior and to elucidate the intermolecular interactions modulated by halogenation, single crystals of CBr_2B, CBrB, and CBrB-Cl were grown and analyzed using X-ray diffraction. The crystals were obtained via the vapor diffusion method under dark conditions, and their crystallographic parameters are summarized in **Table S1**. As shown in **Figure 3a**, the symmetric CBr_2B molecule exhibits a π-core torsion angle (θ) of 4.25°, along with small dihedral angles (Φ) between the D_NB_ND core and the two outer A units, both measuring less than 2.20°, indicating a high degree of coplanarity. In contrast, the asymmetric CBrB displays similarly small Φ values but features a more twisted central core, with an increased θ value of 7.03°. This torsion is likely due to the significant size difference between the hydrogen and bromine atoms on the *o*-BDP moiety. Notably, CBrB-Cl presents the most planar central core, with the smallest θ value of 1.07° and Φ values around 1.00°, suggesting that the introduction of the Cl-IC unit strengthens intermolecular interactions, thereby influencing the overall molecular conformation.

View Article Online
DOI: 10.1039/D5SC04976H

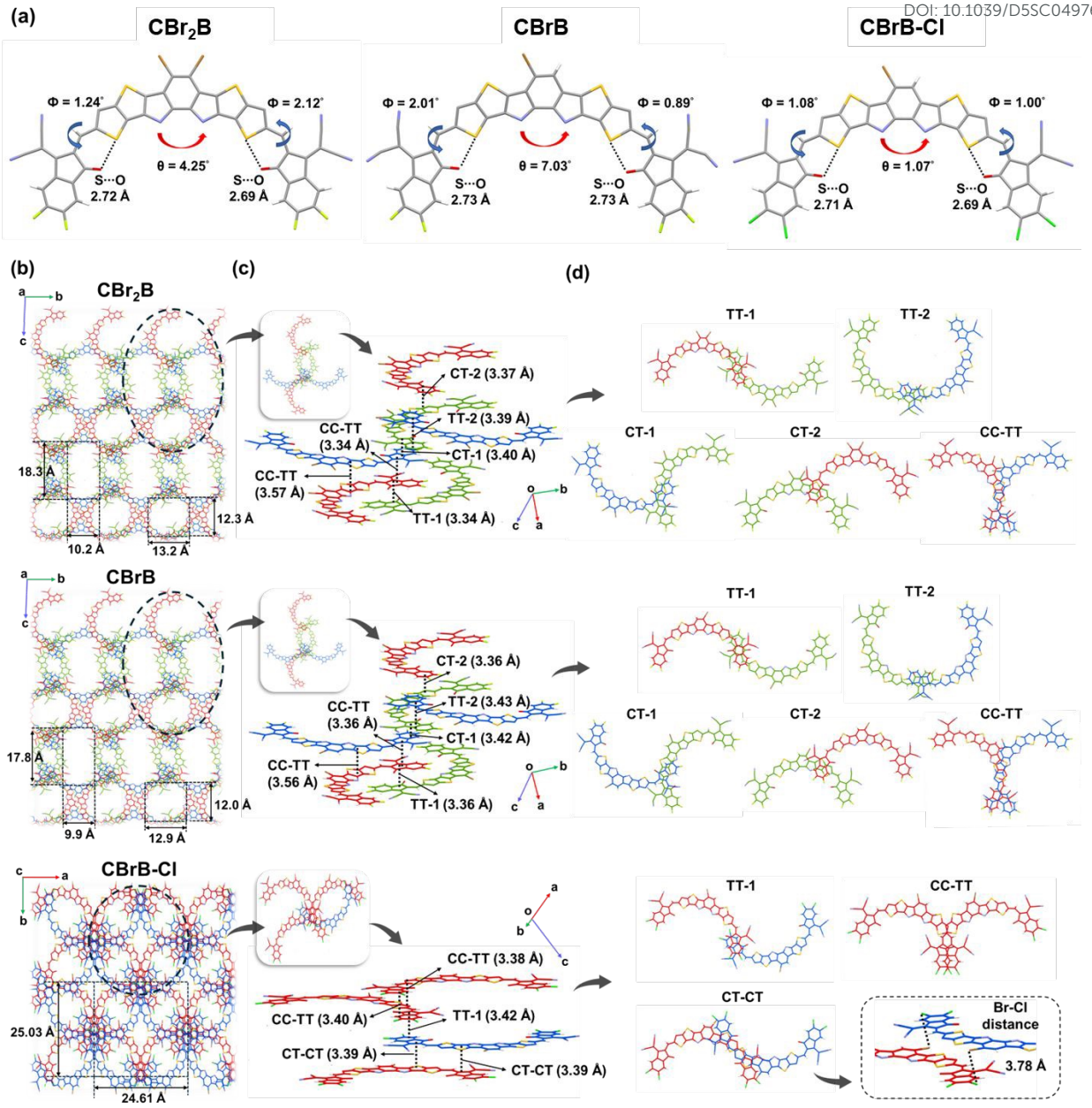

Figure 3. (a) The monomolecular crystallographic structure of CBr_2B, CBrB, and CBrB-Cl single crystals. (b) Top views of the 3D interpenetrating packing patterns of CBr_2B, CBrB, and CBrB-Cl single crystals. (c) Packing arrangements within each unit cell, accompanied by corresponding enlarged side views of CBr_2B, CBrB, and CBrB-Cl single crystals. (d) Dimeric packing modes within each unit cell of CBr_2B, CBrB, and CBrB-Cl single crystals. For clarity, all alkyl side chains and hydrogen atoms are omitted.

Driven by multiple π-π interactions, CBr_2B, CBrB, and CBrB-Cl molecules self-assemble into a grid-like, three-dimensional interpenetrating network, creating multiple pathways for electron

View Article Online
DOI: 10.1039/D5SC04976H

transport (**Figure 3b**). Interestingly, CBr_2B and CBrB exhibit remarkably similar packing characteristics. Within the unit cells of both CBr_2B and CBrB (**Figures 3c** and **3d**), six molecules are accommodated, forming five distinct dimeric packing modes: the S-shaped TT-1 mode (terminal-to-terminal), the U-shaped TT-2 mode, the V-shaped CT-1 mode (core-to-terminal), the M-shaped CT-2 mode, and the Y-shaped CC-TT mode (core-to-core). Notably, in the CC-TT mode of CBr_2B, the two molecules are slightly offset to minimize steric hindrance derived from the four bromine atoms. In contrast, CBrB molecules exhibit a shorter π-π stacking distance and greater overlap in the CC-TT mode. Additionally, the void spaces in the overall packing pattern of CBrB are slightly smaller than those observed in CBr_2B, suggesting a more compact molecular arrangement in the asymmetric NFA. In contrast, CBrB-Cl, featuring a Cl-IC end-group, exhibits dramatic changes in its overall packing pattern (**Figure 3b**). Compared to CBrB, CBrB-Cl displays a kaleidoscope-like packing network with a reduced number of dimeric packing modes, indicative of increased packing order and crystallinity.[25] Within the unit cell of CBrB-Cl **(Figures 3c** and **3d**), only the S-shaped TT-1 mode, M-shaped CC-TT mode, and S-shaped CT-CT modes are observed. The emergence of the CT-CT mode is associated with the Cl-IC unit, which enhances intermolecular interactions between the bromine atom on the central unit and the chlorine atom on the terminal group. The bromine-chlorine short contact approximates the sum of the van der Waals radii of these atoms, suggesting strong non-covalent interactions. In addition, the packing coefficients of the single crystals were calculated using Platon software to further investigate the packing density of the three brominated NFAs. Compared to CBr_2B, which exhibits a packing coefficient of 63.7%, CBrB shows a higher value of 64.7%, indicating a denser overall packing, consistent with its smaller void space as discussed above. Furthermore, CBrB-Cl displays the highest packing coefficient of 66.9% among the three NFAs, suggesting its most tightly packed crystal structure. The formation of CT-CT dimeric packing configurations, strengthened by bromine-chlorine interactions, along with the densely packed and highly ordered structure of CBrB-Cl, is expected to significantly enhance charge transfer efficiency.[41, 42]

View Article Online
DOI: 10.1039/D5SC04976H

2.5 Device characteristics

In this study, OPV devices were fabricated using an inverted architecture (ITO/ZnO/active layer/MoO_3/Ag). PM6 was employed as the p-type donor material, blended with the three NFAs at a weight ratio of 1:1.2. The active layers were prepared by spin-coating PM6:NFA solutions in the non-halogenated solvent *o*-xylene, without adding any additives. The *J*–*V* curves and EQE spectra of the devices are presented in **Figure 4**a, with corresponding photovoltaic parameters summarized in **Table 2**. The PM6:CBr_2B-based device exhibits a high V_{oc} of 0.89 V, an excellent FF of 74.82%, and a moderate J_{sc} of 24.88 mA cm^{-2}, resulting in a PCE of 16.57%. The moderate J_{sc} of the PM6:CBr_2B device is primarily attributed to the blue-shifted absorption range rather than issues with charge dynamics, as evidenced by the high EQE values exceeding 83% across the absorption spectrum of CBr_2B (Figure 4b). CBrB features an asymmetric structure, formed by the removal of one central bromine atom, which enhances the intramolecular charge transfer (ICT) effect, upshifts the LUMO energy level, and red-shifts its absorption spectrum. As a result, the PM6:CBrB-based device exhibits a significantly improved J_{sc} of 25.78 mA cm^{-2}, along with an elevated V_{oc} of 0.90 V and a FF of 74.72%, resulting in an enhanced PCE of 17.28%. Notably, the improvement in J_{sc} is achieved without compromising V_{oc} or FF, highlighting the critical role of carefully tuning the electron-withdrawing ability of *o*-BDP-based NFAs. This advancement, accomplished through precise control of bromination, underscores the great potential of the *o*-BDP central core for molecular design in high-performance inverted OPVs. To estimate the synthetic efficiency, the synthetic complexity (SC) of the new NFA materials were calculated (Schemes S2–S5) and summarized in Table S4.[43] CBrB-Cl shows a lower synthetic complexity of 83.16 compared with Y6 (83.52), CBr_2B (88.19), CBrB (88.56), AQx-2 (91.30) and L8-BO (96.46). Furthermore, figure-of-merit (FOM) defined as PCE/SC were also calculated to incorporate the PCE factor into the evaluation.[44] CBrB-Cl demonstrates the highest FOM value (0.213), surpassing those of Y6 (0.188), L8-BO (0.190), AQx-2 (0.182), CBr_2B (0.188), and CBrB (0.195). The FOM values of our NFAs fall within the range of 0.18–0.21, which is comparable to Y-series NFAs and indicates a good balance between device performance and synthetic complexity.

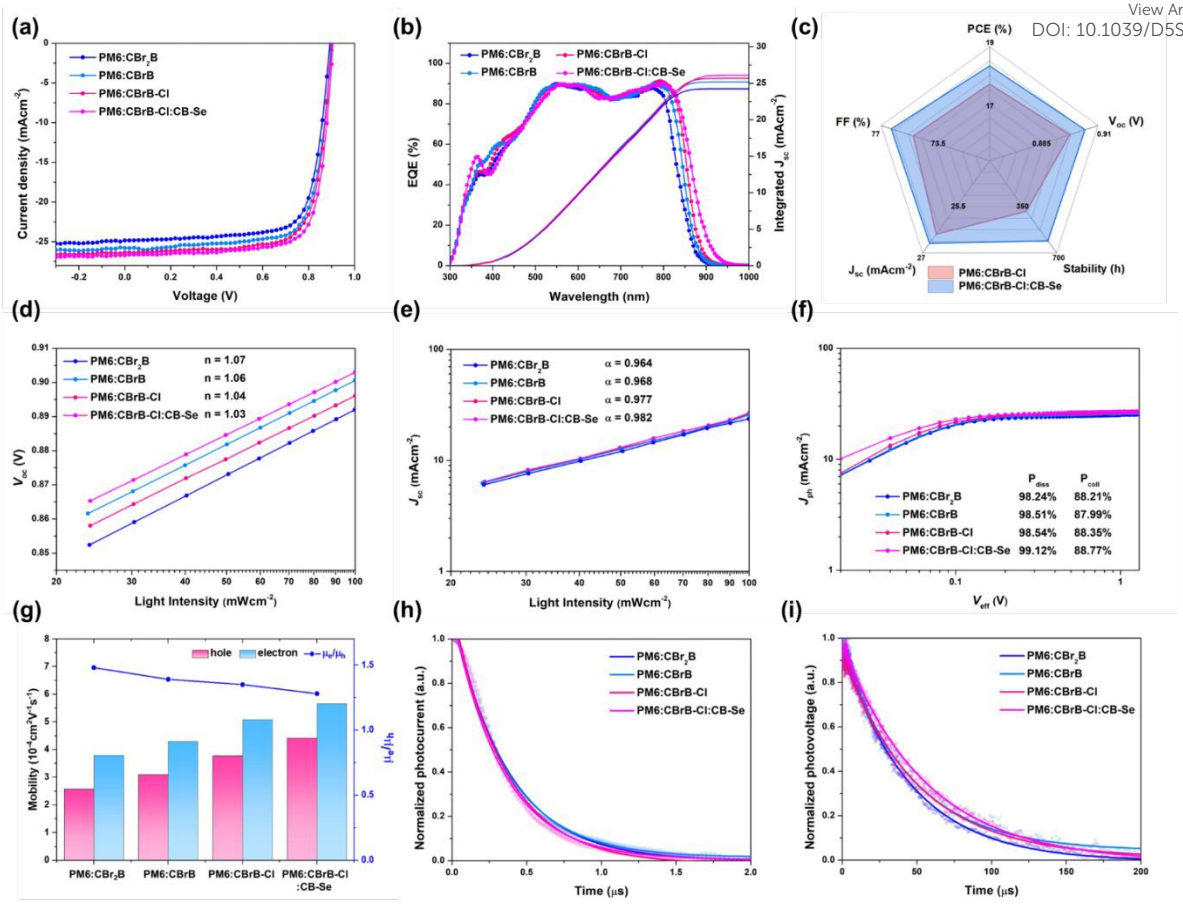

Figure 4. (a) *J-V* curves and (b) EQE spectra of optimized PM6:CBr_2B, PM6:CBrB, PM6:CBrB-Cl and PM6:CBrB-Cl:CB-Se based devices. (c) Radar diagram of the OPV parameters in the PM6:CBrB-Cl:CB-Se device compared with the PM6: CBrB-Cl based device. (d) V_{oc} versus light intensity, (e) J_{sc} versus light intensity and (f) J_{ph} versus V_{eff} diagrams of the optimized binary and ternary devices. (g) Schematic diagram of electron and hole mobilities of the optimized binary and ternary devices obtained by SCLC measurements. (h) Transient photocurrent (TPC) and (i) transient photovoltage (TPV) with their corresponding fitting curves (solid curves) of PM6:CBr_2B, PM6:CBrB, PM6:CBrB-Cl and PM6:CBrB-Cl:CB-Se based devices.

More encouragingly, the PM6:CBrB-Cl-based device achieved an even higher PCE of 17.69%, accompanied by an impressive J_{sc} of 26.39 mA cm^{-2}, while maintaining a V_{oc} of 0.90 V and a high FF of 74.93%. Beyond the red-shifted absorption induced by the Cl-IC unit, the highly ordered packing structure observed in the single crystal of CBrB-Cl likely contributes to the enhanced J_{sc}. Through meticulous molecular design, we thus successfully overcome the typical trade-off between V_{oc} and J_{sc}. Furthermore, the retention of a high V_{oc} despite the deeper LUMO energy level of CBrB-Cl indicates

a significant reduction in energy loss. From CBr_2B to CBrB-Cl, the J_{sc} improves by 6.1% without compromising V_{oc}, demonstrating the effectiveness of our halogen-engineering in fine-tuning the properties of *o*-BDP-based NFAs. Beyond molecular-level engineering, the acceptor alloy strategy has emerged as an effective approach to fine-tune the properties of OPV devices.[37-40] To further enhance device performance, we explored an acceptor alloy system combining CBrB-Cl and CB-Se,[25] both asymmetric *o*-BDP-based NFAs. CB-Se features a slightly higher LUMO energy level and a marginally red-shifted absorption peak relative to CBrB-Cl, while both share similar optimal thermal annealing window with PM6 at around 160 °C.[25] These complementary characteristics make CB-Se an ideal alloying component with CBrB-Cl to optimize the active layer morphology and electronic properties. Utilizing the non-halogenated solvent *o*-xylene, the optimized PM6:CBrB-Cl:CB-Se (1:0.9:0.3) acceptor alloy delivered a remarkable PCE of 18.33%, accompanied by a significantly enhanced FF of 76.35% and simultaneous improvements in V_{oc} of 0.904 V and J_{sc} of 26.69 mA cm^{-2}. All the key parameters of the ternary device apparently surpass those of the binary PM6:CBrB-Cl device as shown in the radar diagram in Figure 4c. The results demonstrate that carefully engineered acceptor alloys synergistically optimize charge generation, transport, and collection, ultimately leading to enhanced device efficiency. The PCE of 18.33% ranks among the highest reported for inverted devices without any ZnO treatment, as shown in Table S8. It should also be noted that the Se atom in CB-Se, which can enhance intermolecular interactions and promote denser packing within the acceptor alloy system, may contribute to the improvement of the active-layer morphology.[25] The dielectric constants of the blend films of asymmetric NFAs, PM6:CBrB, PM6:CBrB-Cl, and PM6:CBrB-Cl:CB-Se were measured to be 3.86, 4.14, and 4.23, respectively, aligning well with the trend in dipole moment and the trend of ε_r of the neat films. The enhanced device performance closely correlates with the increasing ε_r, indicating the critical role of bulk dielectric properties in charge dissociation and transport.[8-10] However, although the PM6:CBr_2B blend exhibits a higher dielectric constant ($\varepsilon_r = 4.02$) than PM6:CBrB, its limited absorption range constrains the overall device performance.

View Article Online
DOI: 10.1039/D5SC04976H

Table 2. Optimized device parameters for the binary and ternary OPVs.

Active layer	Blend ratio in wt%	V_{oc} [V]	J_{sc} [mA cm^{-2}]	$J_{sc,\ EQE}$ [mA cm^{-2}] (error %)	FF [%]	PCE [%]
PM6:CBr_2B	1:1.2	0.892 (0.896 ± 0.004)	24.88 (24.57 ± 0.26)	24.24 (2.57)	74.82 (74.59 ± 0.47)	16.57 (16.40 ± 0.12)
PM6:CBrB	1:1.2	0.901 (0.897 ± 0.003)	25.78 (25.73 ± 0.14)	25.19 (2.23)	74.72 (74.53 ± 0.35)	17.28 (17.115 ± 0.10)
PM6:CBrB-Cl	1:1.2	0.897 (0.896 ± 0.007)	26.39 (26.22 ± 0.13)	25.67 (2.28)	74.93 (74.78 ± 0.54)	17.69 (17.54 ± 0.10)
PM6:CBrB-Cl:CB-Se	1:0.9:0.3	0.904 (0.899 ± 0.003)	26.69 (26.84 ± 0.12)	26.11 (2.17)	76.35 (75.01 ± 0.70)	18.33 (18.04 ± 0.19)

2.6 Charge dynamics analysis

To gain deeper insight into charge recombination behavior, we investigated the dependence of light intensity (P_{light}) on both V_{oc} and J_{sc}. The corresponding results are presented in Figure 4d and 4e. The relationship between J_{sc} and P_{light} can be described by the power-law equation $J_{sc} \propto (P_{light})^{\alpha}$, where the exponent α serves as an indicator of bimolecular recombination. The α value is determined from the slope of the logarithmic plot of J_{sc} versus P_{light}. An α value close to 1 suggests minimal bimolecular recombination, indicative of efficient charge transport.[45, 46] On the other hand, the dependence of V_{oc} on P_{light} follows the relationship $V_{oc} \propto n(kT/q)\ln(P_{light})$, where n is the ideality factor, k is the Boltzmann constant, T is the absolute temperature, and q is the elementary charge. An n value close to 1 indicates less trap-assisted recombination.[47] The α values for the binary systems PM6:CBr_2B, PM6:CBrB, and PM6:CBrB-Cl are 0.964, 0.968, and 0.977, respectively, which are also very close to 1. This indicates that bimolecular recombination is effectively suppressed across all three systems. Similarly, the ideality factors (n value) for these blends are also close to 1, with values of 1.07 for PM6:CBr_2B, 1.06

View Article Online
DOI: 10.1039/D5SC04976H

for PM6:CBrB, and 1.04 for PM6:CBrB-Cl, indicating that trap-assisted recombination is efficiently suppressed in the binary systems. Notably, the PM6:CBrB-Cl-based device exhibits α and n values closest to 1, signifying the most effective suppression of both bimolecular and trap-assisted recombination and highlighting the significant effects of increasing dielectric constant in decreasing charge recombination rates. This, combined with its most redshifted absorption spectrum, contributes to the highest J_{sc} of 26.39 mA cm^{-2} among the binary devices. The ternary PM6:CBrB-Cl:CB-Se device, with α and n approaching ideal values of 0.982 and 1.03, respectively, exhibits even stronger suppression of recombination processes. The largely suppressed recombination, which may result from the large dielectric constant of both CBrB-Cl and CB-Se, along with the complementary absorption characteristics of CBrB-Cl and CB-Se, synergistically leads to an even higher J_{sc} of 26.69 mA cm^{-2}. The relationship between photocurrent density (J_{ph}) and effective voltage (V_{eff}) was evaluated to elucidate the charge dissociation and collection characteristics of the OPVs.[48] The exciton dissociation efficiency (P_{diss}) is determined by the ratio of J_{sc} to the saturated current density (J□$_a$□), while the charge collection efficiency (P_{coll}) is defined as the ratio of J□$_{ax}$ to J□$_a$□. As illustrated in Figure 4f, all OPV devices exhibited high P_{diss} values exceeding 98%, indicating efficient exciton dissociation. PM6:CBrB-Cl showed a higher P_{coll} of 88.35% compared to the PM6:CBr$_2$B and PM6:CBrB systems, suggesting that more efficient charge collection also contributes to its higher J_{sc} and PCE. Furthermore, with the incorporation of CB-Se, the ternary PM6:CBrB-Cl:CB-Se device exhibited the highest P_{diss} of 99.12% and P_{coll} of 88.77%.

Additionally, hole-only and electron-only devices were fabricated to evaluate hole and electron mobilities through space-charge-limited current (SCLC) measurements.[48] The calculated hole (μ□) and electron (μ_e) mobilities are $2.57 \times 10^{-4}/3.79 \times 10^{-4}$, $3.10 \times 10^{-4}/4.31 \times 10^{-4}$, and $3.77 \times 10^{-4}/5.08 \times 10^{-4}$ cm^2 V^{-1} s^{-1} for PM6:CBr$_2$B, PM6:CBrB, and PM6:CBrB-Cl devices, respectively (Figure 4g). Among these, PM6:CBrB-Cl devices exhibited the highest μ□ and μ_e values, along with the most balanced electron-to-hole mobility ratio of 1.35, which correlates with the highest PCE observed in the binary system. The enhanced mobility can be attributed to the higher crystallinity of CBrB-Cl, as

evidenced by its elevated melting temperature (T□) and the largest Δ λ □$_{ax}$ in the absorption spectra. By incorporating CB-Se into the PM6:CBrB-Cl system, the hole and electron mobilities are further amplified to 4.42×10^{-4} and 5.66×10^{-4} cm² V^{-1} s^{-1}, respectively, with an even more balanced μ_e/μ□ ratio of 1.28. The more balanced μ_e/μ□ PM6:CBrB-Cl:CB-Se device may further contribute to the enhanced J_{sc} and PCE of the devices. The examination of charge extraction time and carrier lifetime provides valuable insights into the charge carrier dynamics of OPVs. To this end, transient photocurrent (TPC) measurements were conducted to determine the charge extraction time, while transient photovoltage (TPV) measurements were used to evaluate the carrier lifetime of the devices.[49] As shown in Figure 4h, the charge extraction times for PM6:CBr_2B, PM6:CBrB, and PM6:CBrB-Cl are 0.37 μs, 0.37 μs, and 0.35 μs, respectively. These small and comparable values indicate efficient charge extraction in all devices. In contrast, the carrier lifetimes follow an ascending trend, with values of 44.87 μs for PM6:CBr_2B, 44.99 μs for PM6:CBrB, and 49.35 μs for PM6:CBrB-Cl. The longer carrier lifetime observed in PM6:CBrB-Cl-based devices suggests better suppression of charge recombination, which contributes to an enhanced charge collection probability (P_{coll}). These advantages in PM6:CBrB-Cl-based devices are further amplified by the incorporation of CB-Se. The ternary PM6:CBrB-Cl:CB-Se device exhibits a synergistic effect, with the shortest charge extraction time of 0.33 μs and an extended carrier lifetime of 55.49 μs. Combined with the complementary absorption characteristics of the two NFAs, these factors lead to improved J_{sc} and PCE.

Additionally, time-resolved photoluminescence (TRPL) spectroscopy was employed to investigate the exciton lifetimes in the NFA neat films. The CBr_2B and CBrB films exhibited similar exciton lifetimes of approximately 0.6 ns (Figure S6).[50, 51] In contrast, the CBrB-Cl film showed a slightly prolonged exciton lifetime of 0.65 ns, which may contribute to the enhanced exciton dissociation observed in the corresponding devices. Notably, the CBrB-Cl:CB-Se film exhibited a significantly longer exciton lifetime of ~0.79 ns, likely attributed to the heavy atom effect.

The charge dynamics of the PM6:CBrB-Cl:CB-Se blend were further explored using femtosecond transient absorption spectroscopy (fs-TAS) to elucidate the impact of the acceptor alloy

system on exciton-to-charge transition dynamics.[52-54] For these experiments, the PM6:CBrB-Cl, PM6:CB-Se and PM6:CBrB-Cl:CB-Se blends were deposited onto quartz substrates, excited at around 810 nm (targeting acceptors), and probed between 600 and 1000 nm. Upon excitation, all blend films exhibit a negative ground state bleaching (GSB) signal of acceptors at ~820 nm and a positive localized exciton (LE) signal at ~930 nm (Figure 5a-c, Figure S7), consistent with the features observed in neat films (Figure S8). Simultaneously, another negative signal appears at ~640 nm in all blend films, assigned to the GSB signal of PM6, indicating an ultrafast hole transfer process from acceptor to donor.

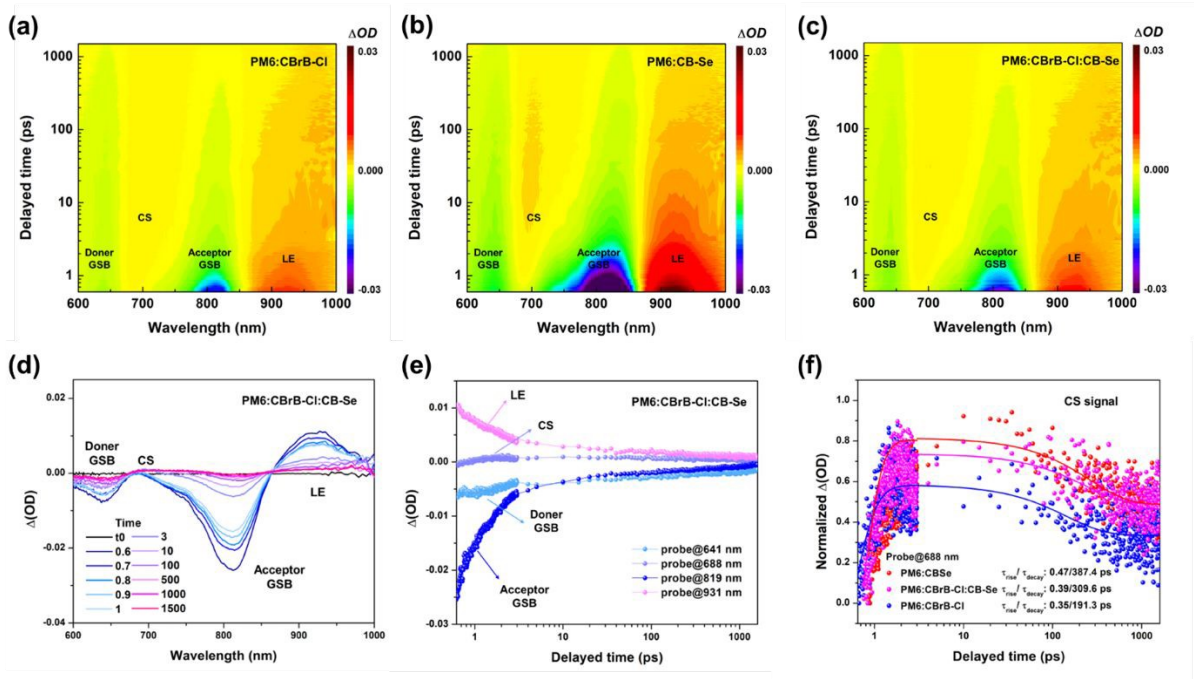

Figure 5. Two-dimensional color plots of transient absorption spectra (TAS) for (a) PM6:CBrB-Cl, (b) PM6:CB-Se, and (c) PM6:CBrB-Cl:CB-Se blend films. (d) TAS of the PM6:CBrB-Cl:CB-Se blend at selected delay times.(e) Kinetic traces at selected probe wavelengths for the PM6:CBrB-Cl:CB-Se blend. (f) Charge separation (CS) signal rise and decay dynamics for PM6:CBrB-Cl, PM6:CB-Se, and PM6:CBrB-Cl:CB-Se blend films.

As the GSB signal of PM6 decays, a new positive signal emerges at ~690 nm, indicating the formation of the charge-separated (CS) state.[52-54] To analyze the CS dynamics, its rise and decay characteristics were fitted. The PM6:CBrB-Cl film exhibits a faster CS signal rise time constant (τ_{rise}

View Article Online
DOI: 10.1039/D5SC04976H

= 0.35 ps) and a shorter decay time constant (τ_{decay} = 191 ps), while PM6:CB-Se shows a slower τ_{rise} = 0.47 ps but a longer τ_{decay} = 387 ps. A faster rise time suggests more efficient charge separation, whereas a longer decay time indicates extended carrier lifetime and suppressed bimolecular charge recombination.[53, 54] The alloy-type PM6:CBrB-Cl:CB-Se film effectively integrates the advantages of both CBrB-Cl and CB-Se, achieving balanced CS characteristics with a faster τ_{rise} = 0.39 ps and a longer τ_{decay} = 309 ps, synergistically enhancing J_{sc} and FF in the ternary system.

2.7 Energy Loss analysis

To gain insights into the well-maintained V_{oc} from CBr_2B to CBrB-Cl, an energy loss (E_{loss}) analysis of the OPVs was conducted. The total E_{loss} is defined as the difference between the optical bandgap (E_g) and qV_{oc} ($E_{loss} = E_g - qV_{oc}$), where E_g is determined from normalized FTPS-EQE and electroluminescence (EL) spectra (**Figure 6**a–c).[55, 56] The E_g values of CBr_2B, CBrB, and CBrB-Cl decrease progressively from 1.480 eV to 1.468 eV and 1.451 eV, respectively, consistent with the red-shifted absorption profiles of these NFAs. Correspondingly, the E_{loss} values exhibit a declining trend of 0.584, 0.571, and 0.555 eV for PM6:CBr_2B, PM6:CBrB, and PM6:CBrB-Cl devices, respectively, suggesting that the simultaneous suppression of E_{loss} is a key factor in overcoming the trade-off between V_{oc} and J_{sc} in PM6:CBrB and PM6:CBrB-Cl-based devices. The total E_{loss} consists of three components: charge generation loss (ΔE_{CT}), radiative recombination loss (ΔE_r), and non-radiative recombination loss (ΔE_{nr}).[57] The charge transfer state energy (E_{CT}) was estimated by fitting the EL and FTPS-EQE spectra (Figure 6a–c), with ΔE_{CT} defined as the energy difference between E_g and E_{CT}.[58, 59] As shown in **Table 3**, ΔE_{CT} values are 0.043, 0.041, and 0.035 eV for PM6:CBr_2B, PM6:CBrB, and PM6:CBrB-Cl, respectively. The small energy offset between the local excitation (LE) state and the CT state suggests possible hybridization, which could weaken the coupling between the highest vibrational ground state and the lowest CT state, thereby reducing non-radiative recombination.[60-63] ΔE_{nr} was experimentally determined from EQE_{EL} measurements (Figure 6d) using the equation $\Delta E_{nr} = (kT/q)\ln(1/EQE_{EL})$,[64] yielding values of 0.281, 0.271, and 0.258 eV for PM6:CBr_2B, PM6:CBrB, and

View Article Online
DOI:10.1039/D5SC04976H

PM6:CBrB-Cl devices, respectively. The gradual decrease in ΔE_{nr} aligns with the trend observed in the Stokes shift ($\Delta\lambda_{Stokes}$) of 86, 82 and 70 nm for neat CBr_2B, CBrB, and CBrB-Cl films (Figure 6e), respectively. Since $\Delta\lambda_{Stokes}$ originates from energy losses during internal conversion and vibrational relaxation, a smaller $\Delta\lambda_{Stokes}$ indicates reduced ΔE_{nr}.[26, 65] In addition, we observed that CBr_2B demonstrated the lowest PL intensity (Figure S6a), aligning well with the lowest response in EQE_{EL} measurement and suggesting the existence of the heavy atom effect on CBr_2B. Notably, the suppressed ΔE_{nr} consistent with the decreasing trend in ΔE_{CT}, appears to be the primary factor contributing to the reduced E_{loss} in PM6:CBrB and PM6:CBrB-Cl devices (Figure 6f). Furthermore, the introduction of CB-Se into the PM6:CBrB-Cl blend further reduces ΔE_{nr} to 0.248 eV (Figure S9), resulting in an even lower E_{loss} of 0.542 eV and the highest V_{oc} obtained for the PM6:CBrB-Cl:CB-Se-based device. The enhanced dielectric constant of PM6:CBrB-Cl:CB-Se bulk further corroborates the observed decrease in ΔE_{r}.

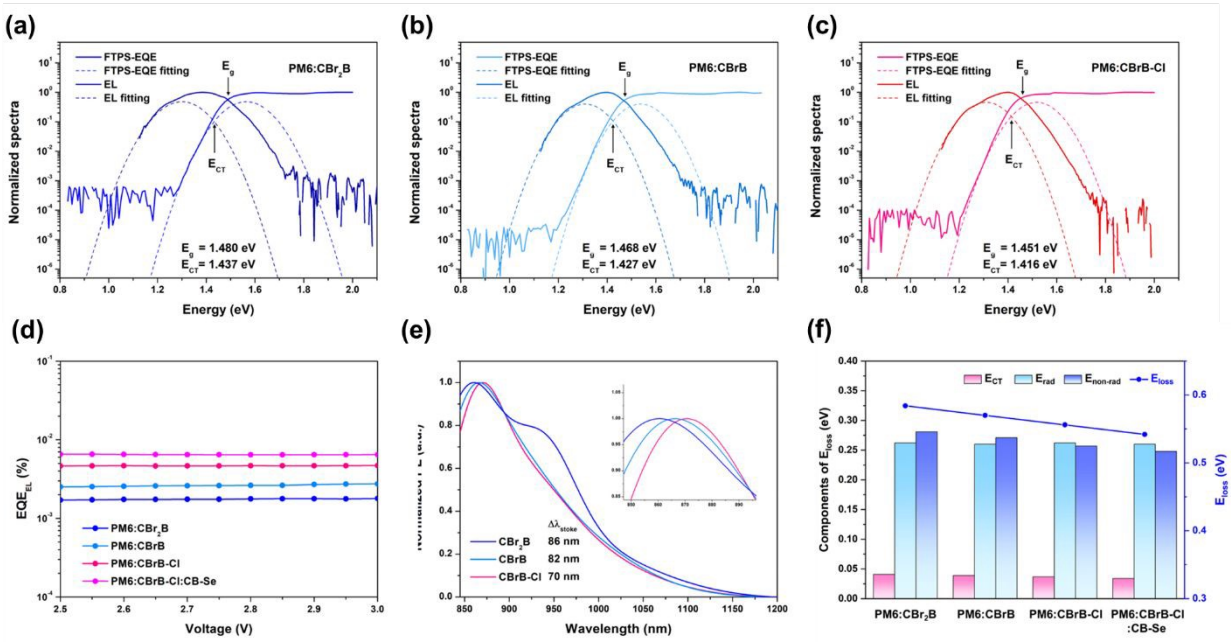

Figure 6. Normalized spectra of EL and FTPS-EQE measurements with the corresponding fitting curves of (a) PM6:CBr_2B, (b) PM6:CBrB and (c) PM6:CBrB-Cl devices. (d) EQE_{EL} spectra of the optimized binary and ternary devices. (e) PL spectra of CBr_2B, CBrB and CBrB-Cl blend films. (f)

Statistical diagram of E_{loss} of PM6:CBr_2B, PM6:CBrB, PM6:CBrB-Cl and PM6:CBrB-Cl:CB-Se devices decomposed into $\Delta E_{CT,}$ ΔE_r and ΔE_{nr} terms.

Table 3. Detailed parameters of energy loss analysis of the binary and ternary OPVs.

Active layer	E_g [eV][a)]	$V_{oc,\,avg}$ [V]	E_{CT} [eV][b)]	ΔE_{CT} [eV][c)]	ΔE_r [V][d)]	ΔE_{nr} [V][e)]	EQE_{EL}	E_{loss} [eV]	E_u [meV][f)]
PM6:CBr_2B	1.480	0.896	1.437	0.043	0.260	0.281	1.75×10^{-5}	0.584	23.97
PM6:CBrB	1.468	0.897	1.427	0.041	0.259	0.271	2.62×10^{-5}	0.571	24.28
PM6:CBrB-Cl	1.451	0.896	1.416	0.035	0.262	0.258	4.67×10^{-5}	0.555	22.81
PM6:CBrB-Cl:CB-Se	1.441	0.899	1.407	0.034	0.260	0.248	6.49×10^{-5}	0.542	22.08

[a)]Bandgap is estimated from the cross-point of normalized FTPS-EQE and EL spectra; [b)]E_{CT} is obtained from the fitting curves of normalized FTPS-EQE and EL spectra; [c)]ΔE_{CT} is determined from the equation: $\Delta E_{CT} = E_g - E_{CT}$; [d)]$\Delta E_r$ was determined from the equation: $\Delta E_r = E_{CT}/q\text{-}V_{oc}\text{-}\Delta E_{nr}$; [e)]$\Delta E_{nr}$ is determined from EQE_{EL} result, which followed the equation: $\Delta E_{nr} = (kT/q)\ln(1/EQE_{EL})$; [f)]$E_u$ is obtained by exponential fitting of low-energy part of the FTPS-EQE spectra.

2.8 Device film morphology analysis

The nanostructure and molecular packing features significantly influence the charge transport and recombination behaviors of OPVs. To investigate these effects, grazing incidence wide-angle X-ray scattering (GIWAXS) experiments were conducted on neat NFAs and their blend films with PM6. The resulting 2D diffraction patterns and corresponding 1D profiles in the out-of-plane (q_z) and in-plane (q_{xy}) directions are presented in **Figure 7**. In the 2D GIWAXS patterns of all neat films, a strong and distinct π–π stacking (010) diffraction peak was observed in the q_z direction, indicating a predominant face-on orientation for the NFAs, favorable for efficient charge transport. Compared to CBrB and CBr_2B, which exhibited similar π–π stacking distances (d_π) of 3.59 Å and crystalline coherence lengths ($L_{c\,\pi\text{-}\pi}$) of 15.28 Å and 15.71 Å, respectively, the CBrB-Cl film showed a slightly reduced d_π of 3.57 Å

and an increased $L_{c\ \pi\text{-}\pi}$ of 17.14 Å. This suggests that the chlorinated IC unit enhances molecular packing interactions.[7]

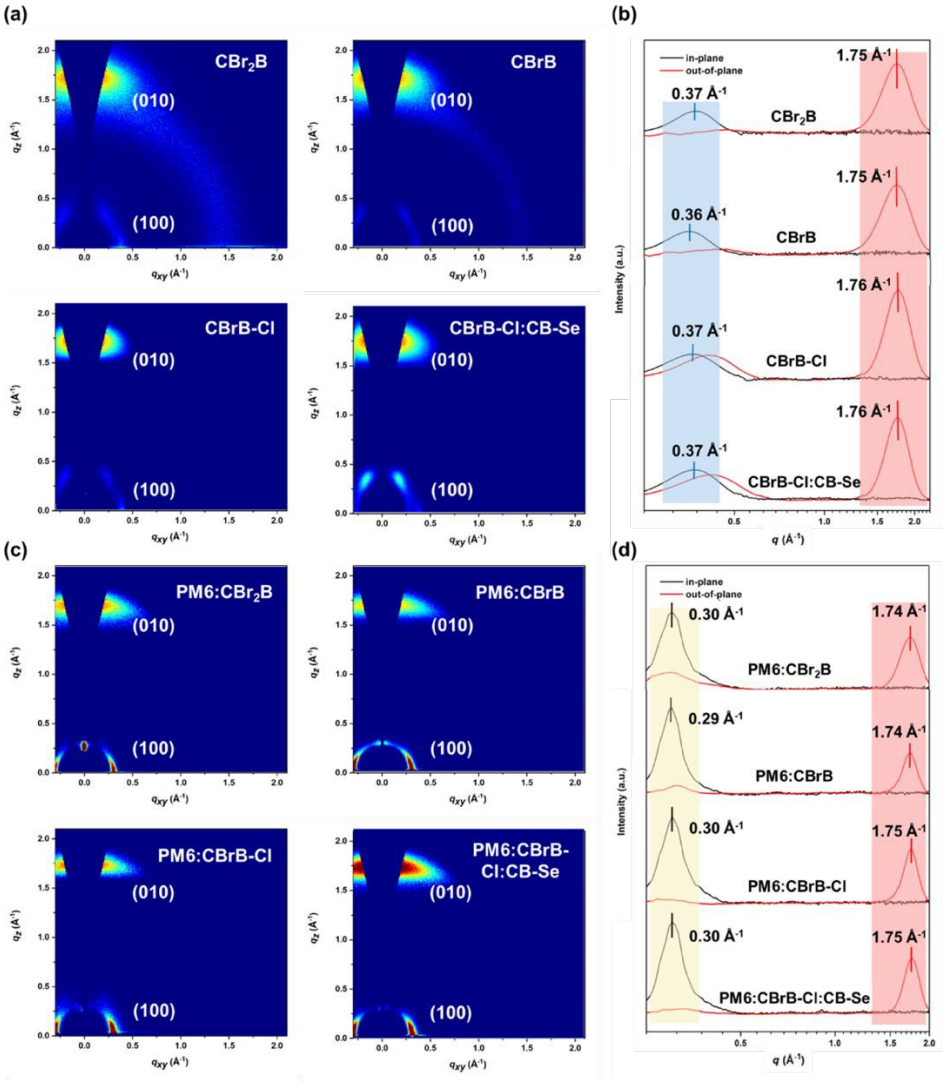

Figure 7. (a) 2D GIWAXS patterns of CBr_2B, CBrB, CBrB-Cl and CBrB-Cl:CB-Se films and (b) their corresponding 1D profiles extracted in out-of-plane and in-plane directions. (c) 2D GIWAXS patterns of PM6:CBr_2B, PM6:CBrB, PM6:CBrB-Cl and PM6:CBrB-Cl:CB-Se blend films and (d) their corresponding 1D profiles extracted in out-of-plane and in-plane directions.

Interestingly, the CBrB-Cl:CB-Se blend film also displayed a prominent (010) peak in the q_z direction, with a similarly small d_π of 3.57 Å and an even larger $L_{c\ \pi\text{-}\pi}$ of 18.24 Å. These results indicate that the double asymmetric CBrB-Cl:CB-Se blend forms a compatible acceptor alloy with higher crystallinity.[37] PM6:CBrB and PM6:CBr_2B exhibited not only strong diffraction peaks at q_{xy} = 0.3

View Article Online
DOI: 10.1039/D5SC04976H

Å^{-1} but also weak peaks at q_z around 0.3 Å^{-1}, indicating the side-chain lamellar packing of PM6 in both face-on and edge-on orientations. In contrast, PM6:CBrB-Cl and PM6:CBrB-Cl:CB-Se blends displayed solely strong lamellar peaks at q_{xy} = 0.3 Å^{-1}, suggesting a predominant face-on lamellar packing. Simultaneously, the π–π stacking peaks in the q_z direction of the blend films closely resemble those observed in the neat NFA films, centered at 1.74, 1.74, 1.75 and 1.75 Å^{-1} for the PM6:CBrB, PM6: CBr_2B, and PM6:CBrB-Cl, PM6:CBrB-Cl:CB-Se blends, respectively, corresponding to gradually decreasing d_π of 3.61 Å, 3.61 Å, 3.59 Å and 3.59 Å, consistent with the trend observed in the neat films. In the ternary PM6:CBrB-Cl:CB-Se system, the incorporation of CB-Se led to a significant increase in the $L_{c\ \pi\text{-}\pi}$, reaching 25.70 Å. This enhancement indicates improved molecular packing order within the ternary blend, which likely contributes to enhanced charge transport dynamics, ultimately benefiting device performance.[37] Furthermore, the Urbach energy (E_u) for each blend was determined by exponential fitting of the FTPS-EQE spectrum,[49] yielding values of 23.97 meV for PM6:CBr_2B, 24.28 meV for PM6:CBrB, 22.81 meV for PM6:CBrB-Cl, and 22.08 meV for PM6:CBrB-Cl:CB-Se films (Figure S10). The lower E_u of PM6:CBr_2B and PM6:CBrB-Cl compared to PM6:CBrB indicates a more ordered molecular packing in these two blends,[49, 66] which is consistent with the GIWAXS results. The smallest E_u observed in PM6:CBrB-Cl:CB-Se film further confirms the enhanced packing order induced by CB-Se incorporation in the acceptor alloy. [49]

Table 4. The structural parameters deduced from GIWAXS patterns of the neat NFA films and their blend films with PM6. The parameter q_z and q_{xy} indicate the peak centers in in-plane and out-of-plane directions, respectively, and their corresponding d_l and d_π values listed. Crystalline coherence length, L_c, are derived from the full-width at half-maximum (FWHM) δq using the Scherrer equation with shape factor 0.9.

film	In-plane reflection peak				Out-of-plane reflection peak			
	q_{xy}[Å^{-1}]	d_l[Å]	δq_{xy}[Å^{-1}]	L_C[Å]	q_z[Å^{-1}]	d_π[Å]	δq_z[Å^{-1}]	L_C[Å]
CBr_2B	0.37	16.98	0.12	47.12	1.75	3.59	0.36	15.71
CBrB	0.36	17.45	0.11	51.54	1.75	3.59	0.37	15.28
CBrB-Cl	0.37	16.98	0.13	43.50	1.76	3.57	0.33	17.14

CBrB-Cl:CB-Se	0.37	16.98	0.13	43.50	1.76	3.57	0.31	18.24
PM6:CBr_2B	0.30	20.94	0.06	94.25	1.74	3.61	0.24	23.56
PM6:CBrB	0.29	19.50	0.06	94.25	1.74	3.61	0.25	22.62
PM6:CBrB-Cl	0.30	20.94	0.06	94.25	1.75	3.59	0.23	24.59
PM6:CBrB-Cl:CB-Se	0.30	20.94	0.06	94.25	1.75	3.59	0.22	25.70

2.9 Device stability

The thermal stability of the thin films was evaluated using inverted devices subjected to thermal heating at 85 °C under dark conditions and the normalized PCEs as a function of heating time are presented in **Figure 8a**. After 400 h of thermal annealing, the PM6:CBrB-Cl:CB-Se-based device demonstrated superior thermal stability, maintaining over 90% of its initial PCE, compared to other binary devices exhibiting a steeper decline in PCE. The thermal stability follows the trend: PM6:CBrB-Cl:CB-Se > PM6:CBrB-Cl > PM6:CBr_2B > PM6:CBrB. To investigate the effect of central bromination on surface morphology with or without heating, atomic force microscopy (AFM) was performed (**Figure 8b-d**). As shown in **Figure S11**, all neat films of the brominated NFAs exhibited very smooth surfaces with root-mean-square roughness (R_{rms}) values smaller than 1 nm. When blended with PM6, distinct fibrillar structures were observed in all three binary blends, suggesting that the NFAs form favorable morphologies with PM6, which likely contributes to the good FF observed in the corresponding devices. The R_{rms} values of the blends follow the trend: PM6:CBrB-Cl:CB-Se (R_{rms} = 1.72 nm) > PM6:CBrB-Cl (R_{rms} = 1.41 nm) > PM6:CBr_2B (R_{rms} = 1.35 nm) > PM6:CBrB (R_{rms} = 1.22 nm), consistent with the trend in $L_{c\ \pi\text{-}\pi}$ observed from GIWAXS measurements. This correlation indicates that the introduction of additional bromine atom or the substitution with a chlorinated IC unit enhances the material's crystallinity. Furthermore, the ternary PM6:CBrB-Cl:CB-Se blend exhibited an increased R_{rms} of 1.72 nm with a more pronounced fibrillar structure. This suggests that CB-Se incorporation promotes high crystallinity of the blend. Interestingly, after thermal aging at 85 °C for 400 h, the R_{rms} values displayed an inverted trend: 4.85 nm for PM6:CBrB, 3.08 nm for PM6:CBr_2B, 2.27 nm for PM6:CBrB-Cl, and 2.15 nm for PM6:CBrB-Cl:CB-Se-based films (Figure 8b-d). The

View Article Online
DOI: 10.1039/D5SC04976H

higher crystallinity of the blends can maintain more stable surface morphology upon thermal heating, leading to the minimal changes in R_{rms} for PM6:CBrB-Cl and PM6:CBrB-Cl:CB-Se blends.

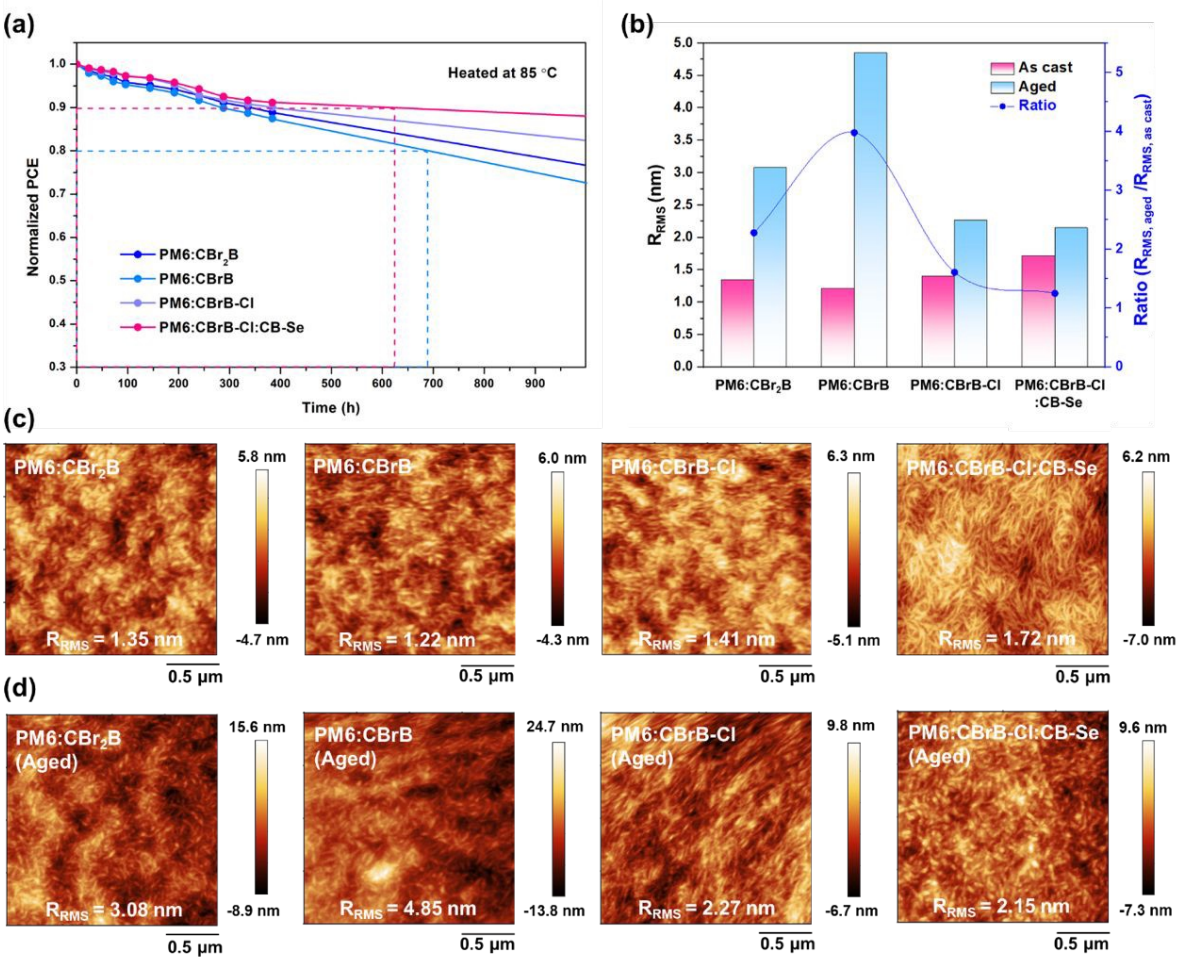

Figure 8. (a) Normalized PCE evolution of PM6:CBr_2B, PM6:CBrB, PM6:CBrB-Cl, and PM6:CBrB-Cl:CB-Se-based devices during thermal aging at 85 °C. (b) Schematic representation of R_{rms} changes in the blend films before and after annealing, along with the corresponding change ratios. (c) AFM images of as-cast PM6:CBr_2B, PM6:CBrB, PM6:CBrB-Cl, and PM6:CBrB-Cl:CB-Se blend films before annealing, and (d) after 400 h of thermal aging.

To further elucidate the high thermal stability of the PM6:CBrB-Cl:CB-Se blend and confirm the formation of the acceptor alloy, we investigated the UV-Vis deviation metric (DM_T)[67-69] results of CBrB-Cl, CB-Se, and CBrB-Cl:CB-Se (3:1 in wt%) to determine the T_g of each film. Among the two acceptors, CBrB-Cl exhibits a higher T_g (124.11 ˚C) than CB-Se (112.96 ˚C), following the same trend as their melting temperatures (T_m). Surprisingly, despite the relatively lower T_g of CB-Se,

incorporating CB-Se into CBrB-Cl (33 wt%) led to an even higher T_g of 133.27 °C for the blend film, indicating enhanced intermolecular interactions and the formation of the alloy phase (Figure S12).[39, 40] This result aligns with literature reports suggesting that the presence of an alloy phase can increase T_g.[39, 40] The higher T_g of CBrB-Cl:CB-Se may improve resistance to thermal stress, contributing to improved morphological stability and sustained device performance under thermal aging conditions.[68, 70]

The Flory–Huggins interaction parameter (χ), derived from contact angle measurements (Figure S13), serves as an effective indicator for evaluating the miscibility between donor–acceptor (D–A) and acceptor–acceptor (A_1–A_2) pairs. As listed in Table S6, the χ values between PM6 and CBr_2B, CBrB, and CBrB-Cl are 0.27, 0.28, and 0.22, respectively. These results suggest that all three NFAs exhibit good miscibility with PM6, which contributes to the formation of well-defined fibrillar surface morphologies and high fill factors (FF) in the corresponding devices.[71] The introduction of bromine atoms enhances the intermolecular interactions between the NFAs and PM6, thereby promoting favorable blend morphology and device performance. Furthermore, the χ value between CBrB-Cl and CB-Se is remarkably low (0.03 K), indicating excellent compatibility between these two asymmetric acceptors. This result confirms that CB-Se is an effective third component in the ternary blend, and the good miscibility between CBrB-Cl and CB-Se is the key factor for the formation of the compatible acceptor alloy.

Conclusion

In conclusion, we have conducted a comprehensive study to understand the relationship between the dielectric constant and molecular structure of acceptor materials, which is crucial for elucidating the charge dynamics and mitigating the energy losses in OPVs. Mono/dibrominated A-D_NB_ND-A-type acceptors, CBr_2B, CBrB and CBrB-Cl, were synthesized efficiently through nitrogen-directing bromination of the central *o*-benzodipyrrole core. The incorporation of a bromine atom with moderate electronegativity and high polarizability at the central core endows CBrB-Cl with the most red-shifted absorption spectrum and the highest ε_r of 3.92 among the series. Besides, CBrB-Cl, featuring Cl···Br

View Article Online
DOI: 10.1039/D5SC04976H

non-covalent interactions, forms a kaleidoscope-like 3D structure with enhanced crystallinity. As a result, the PM6:CBrB-Cl binary device achieved the highest PCE of 17.69% with a high J_{sc} of 26.39 mA cm^{-2}, while maintaining a V_{oc} of 0.90 V and a high FF of 74.93%. Another asymmetric acceptor, CB-Se, including a highly polarizable selenium atom in the core, was introduced as the second acceptor. Both CBrB-Cl and CB-Se share an optimal thermal annealing temperature of approximately 160 °C, enabling the formation of a dual asymmetric acceptor alloy with favorable morphology and enhanced crystallinity. The combination of heavy bromine and selenium atoms in the CBrB-Cl:CB-Se alloy further enhances the overall ε_r of 4.23 of the PM6:CBrB-Cl:CB-Se blend film, which in turn reduces exciton binding energy, promotes efficient charge separation, and suppresses charge recombination, as evidenced by a faster charge separation time (τ_{rise} = 0.39 ps) and a longer charge lifetime (τ_{decay} = 309 ps). As a result, the inverted PM6:CBrB-Cl:CB-Se device exhibits a simultaneously improved J_{sc} of 26.69 mA cm^{-2}, a V_{oc} of 0.904 V, and an FF of 76.35%, yielding a remarkable PCE of 18.33%, which is one of the highest among the inverted devices. The fabrication of the devices was carried out by non-chlorinated solvent, which meet the needs for avoiding using toxic processing solvents. Moreover, the selenium-incorporated CB-Se, with strengthened bromine-selenium interactions, raises the T_g of the CBrB-Cl:CB-Se acceptor alloy, providing excellent device stability against thermal aging at 85°C. Bromine engineering has proven to be a simple and promising strategy for imparting exceptional photovoltaic properties among CB-based analogues. The mono- and di-brominated *o*-benzodipyrrole cores readily undergo efficient coupling reactions, enabling the construction of extended π-conjugated systems from the *o*-BDP scaffold.

Acknowledgements

This work is supported by National Science and Technology Council, Taiwan (grant No. 113-2221-E-A49-001 and 113-2113-M-A49-015-MY3) and Ministry of Education, Taiwan (SPROUT Project-Center for Emergent Functional Matter Science of National Yang Ming Chiao Tung University). We thank the National Center of High-Performance Computing (NCHC) in Taiwan for computer time and

View Article Online
DOI: 10.1039/D5SC04976H

facilities. GIWAXS measurement supports from TPS 25 beamlines of the National Synchrotron Radiation Research Center (NSRRC) are acknowledged; special thank goes to Dr. Yi-Wei Tsai on the GIWAXS data processing.

Conflicts of Interest

There are no conflicts to declare.

Data Availability Statement:

The data that supports the findings of this study are available in the manuscript and Supporting Information of this article. The X-ray crystallographic coordinates for structures of CBr_2B, CBrB and CBrB-Cl have been deposited at the Cambridge Crystallographic Data Centre (CCDC) with CCDC number 2452218, 2452219 and 2452220.

Received: ((will be filled in by the editorial staff))

Revised: ((will be filled in by the editorial staff))

Published online: ((will be filled in by the editorial staff))

References

1. J. Yuan, Y. Zhang, L. Zhou, G. Zhang, H.-L. Yip, T.-K. Lau, X. Lu, C. Zhu, H. Peng, P. A. Johnson, M. Leclerc, Y. Cao, J. Ulanski, Y. Li and Y. Zou, Single-Junction Organic Solar Cell with over 15% Efficiency Using Fused-Ring Acceptor with Electron-Deficient Core, *Joule*, 2019, **3**, 1140-1151.
2. C. Li, J. Zhou, J. Song, J. Xu, H. Zhang, X. Zhang, J. Guo, L. Zhu, D. Wei, G. Han, J. Min, Y. Zhang, Z. Xie, Y. Yi, H. Yan, F. Gao, F. Liu and Y. Sun, Non-fullerene acceptors with branched side chains and improved molecular packing to exceed 18% efficiency in organic solar cells, *Nat. Energy*, 2021, **6**, 605-613.
3. Z. Abbas, S. U. Ryu, M. Haris, C. E. Song, H. K. Lee, S. K. Lee, W. S. Shin, T. Park and J.-C. Lee, Optimized vertical phase separation via systematic Y6 inner side-chain modulation for non-halogen solvent processed inverted organic solar cells, *Nano Energy*, 2022, **101**.
4. S. Zahra, S. Lee, M. Jahankhan, M. Haris, D. H. Ryu, B. J. Kim, C. E. Song, H. K. Lee, S. K. Lee and W. S. Shin, Inner/Outer Side Chain Engineering of Non-Fullerene Acceptors for Efficient Large-Area Organic Solar Modules Based on Non-Halogenated Solution Processing in Air, *Adv. Sci.*, 2024, **11**, e2405716.

5. L. Wang, C. Guo, X. Zhang, S. Cheng, D. Li, J. Cai, C. Chen, Y. Fu, J. Zhou, H. Qin, D. Liu and T. Wang, Alkyl Chain Tuning of Non-fullerene Electron Acceptors toward 18.2% Efficiency Binary Organic Solar Cells, *Chem. Mater.*, 2021, **33**, 8854-8862.
6. H. Chen, H. Liang, Z. Guo, Y. Zhu, Z. Zhang, Z. Li, X. Cao, H. Wang, W. Feng, Y. Zou, L. Meng, X. Xu, B. Kan, C. Li, Z. Yao, X. Wan, Z. Ma and Y. Chen, Central Unit Fluorination of Non-Fullerene Acceptors Enables Highly Efficient Organic Solar Cells with Over 18 % Efficiency, *Angew. Chem. Int. Ed. Engl.*, 2022, **61**, e202209580.
7. Y. Zou, H. Chen, X. Bi, X. Xu, H. Wang, M. Lin, Z. Ma, M. Zhang, C. Li, X. Wan, G. Long, Y. Zhaoyang and Y. Chen, Peripheral halogenation engineering controls molecular stacking to enable highly efficient organic solar cells, *Energy Environ. Sci.*, 2022, **15**, 3519-3533.
8. X. Zhang, C. Li, J. Xu, R. Wang, J. Song, H. Zhang, Y. Li, Y.-N. Jing, S. Li, G. Wu, J. Zhou, X. Li, Y. Zhang, X. Li, J. Zhang, C. Zhang, H. Zhou, Y. Sun and Y. Zhang, High fill factor organic solar cells with increased dielectric constant and molecular packing density, *Joule*, 2022, **6**, 444-457.
9. J. Dong, Y. Li, C. Liao, X. Xu, L. Yu, R. Li and Q. Peng, Dielectric constant engineering of nonfullerene acceptors enables a record fill factor of 83.58% and a high efficiency of 20.80% in organic solar cells, *Energy Environ. Sci.*, 2025, **18**, 4982-4995.
10. H. Fang, Q. Chen, Y. Lin, X. Xu, J. Wang, M. Li, C. Xiao, C. R. McNeill, Z. Tang, Z. Lu and W. Li, Fullerene-Hybridized Fused-Ring Electron Acceptor with High Dielectric Constant and Isotropic Charge Transport for Organic Solar Cells, *Angew. Chem. Int. Ed. Engl.*, 2025, **64**, e202417951.
11. S. Baroni and R. Resta, Ab initio calculation of the macroscopic dielectric constant in silicon, *Phys. Rev. B*, 1986, **33**, 7017.
12. J. Blakemore, Semiconducting and other major properties of gallium arsenide, *J. Appl. Phys.*, 1982, **53**, R123-R181.
13. R. A. Awni, Z. Song, C. Chen, C. Li, C. Wang, M. A. Razooqi, L. Chen, X. Wang, R. J. Ellingson, J. V. Li and Y. Yan, Influence of Charge Transport Layers on Capacitance Measured in Halide Perovskite Solar Cells, *Joule*, 2020, **4**, 644-657.
14. B. Bernardo, D. Cheyns, B. Verreet, R. D. Schaller, B. P. Rand and N. C. Giebink, Delocalization and dielectric screening of charge transfer states in organic photovoltaic cells, *Nat. Commun.*, 2014, **5**, 3245.
15. B. Fan, W. Gao, X. Wu, X. Xia, Y. Wu, F. R. Lin, Q. Fan, X. Lu, W. J. Li, W. Ma and A. K. Jen, Importance of structural hinderance in performance-stability equilibrium of organic photovoltaics, *Nat. Commun.*, 2022, **13**, 5946.
16. H. Liang, X. Bi, H. Chen, T. He, Y. Lin, Y. Zhang, K. Ma, W. Feng, Z. Ma, G. Long, C. Li, B. Kan, H. Zhang, O. A. Rakitin, X. Wan, Z. Yao and Y. Chen, A rare case of brominated small molecule acceptors for high-efficiency organic solar cells, *Nat. Commun.*, 2023, **14**, 4707.
17. D. Qiu, L. Zhang, H. Zhang, A. Tang, J. Zhang, Z. Wei and K. Lu, Elucidating the effects of

bromine substitution in asymmetric quinoxaline central core-based non-fullerene acceptors on molecular stacking and photovoltaic performances, *J. Mater. Chem. A*, 2025, **13**, 4237-4246.

18. H. Liang, H. Chen, Y. Zou, Y. Zhang, Y. Guo, X. Cao, X. Bi, Z. Yao, X. Wan and Y. Chen, Central unit hetero-di-halogenation of acceptors enables organic solar cells with 19% efficiency, *Chem. Commun.*, 2023, **59**, 13367-13370.
19. Y.-J. Cheng, C.-H. Chen, Y.-J. Ho, S.-W. Chang, H. A. Witek and C.-S. Hsu, Thieno [3, 2-b] pyrrolo donor fused with benzothiadiazolo, benzoselenadiazolo and quinoxalino acceptors: synthesis, characterization, and molecular properties, *Org. Lett.*, 2011, **13**, 5484-5487.
20. Y.-J. Cheng, Y.-J. Ho, C.-H. Chen, W.-S. Kao, C.-E. Wu, S.-L. Hsu and C.-S. Hsu, Synthesis, Photophysical and Photovoltaic Properties of Conjugated Polymers Containing Fused Donor–Acceptor Dithienopyrrolobenzothiadiazole and Dithienopyrroloquinoxaline Arenes, *Macromolecules*, 2012, **45**, 2690-2698.
21. C. He, Y. Pan, Y. Ouyang, Q. Shen, Y. Gao, K. Yan, J. Fang, Y. Chen, C.-Q. Ma, J. Min, C. Zhang, L. Zuo and H. Chen, Manipulating the D:A interfacial energetics and intermolecular packing for 19.2% efficiency organic photovoltaics, *Energy Environ. Sci.*, 2022, **15**, 2537-2544.
22. Z. Luo, R. Ma, Z. Chen, Y. Xiao, G. Zhang, T. Liu, R. Sun, Q. Zhan, Y. Zou, C. Zhong, Y. Chen, H. Sun, G. Chai, K. Chen, X. Guo, J. Min, X. Lu, C. Yang and H. Yan, Altering the Positions of Chlorine and Bromine Substitution on the End Group Enables High-Performance Acceptor and Efficient Organic Solar Cells, *Adv. Energy Mater.*, 2020, **10**.
23. Y. J. Xue, Z. Y. Lai, H. C. Lu, J. C. Hong, C. L. Tsai, C. L. Huang, K. H. Huang, C. F. Lu, Y. Y. Lai, C. S. Hsu, J. M. Lin, J. W. Chang, S. Y. Chien, G. H. Lee, U. S. Jeng and Y. J. Cheng, Unraveling the Structure-Property-Performance Relationships of Fused-Ring Nonfullerene Acceptors: Toward a C-Shaped ortho-Benzodipyrrole-Based Acceptor for Highly Efficient Organic Photovoltaics, *J. Am. Chem. Soc.*, 2024, **146**, 833-848.
24. K. H. Huang, B. H. Jiang, H. C. Lu, Y. J. Xue, C. F. Lu, Y. Y. Chang, C. L. Huang, S. Y. Chien, C. P. Chen and Y. J. Cheng, Electron-Rich Heptacyclic S,N Heteroacene Enabling C-Shaped A-D-A-type Electron Acceptors With Photoelectric Response beyond 1000 Nm for Highly Sensitive Near-Infrared Photodetectors, *Adv. Sci.*, 2025, **12**, e2413045.
25. K. H. Huang, C. C. Tseng, C. L. Tsai, Y. J. Xue, H. C. Lu, C. F. Lu, Y. Y. Chang, C. L. Huang, I. J. Hsu, Y. Y. Lai, Y. P. Zheng, B. H. Jiang, C. P. Chen, S. Y. Chien, U. S. Jeng, C. S. Hsu and Y. J. Cheng, Highly Crystalline Selenium-Substituted C-Shaped Ortho-Benzodipyrrole-Based A-D-A-Type Nonfullerene Acceptor Enabling Solution-Processed Single-Crystal-Like Thin Films for Air-Stable, High-Mobility N-Type Transistors, *Adv. Funct. Mater.*, 2024, **35**.
26. Y. Gong, T. Zou, X. Li, S. Qin, G. Sun, T. Liang, R. Zhou, J. Zhang, J. Zhang, L. Meng, Z. Wei and Y. Li, C-shaped ortho-benzodipyrrole-based acceptors with different electronic effects of top substituents for as-cast green-solvent processed high-performance organic solar cells, *Energy Environ. Sci.*, 2024, **17**, 6844-6855.

27. Y. B. Wang, C. L. Tsai, Y. J. Xue, B. H. Jiang, H. C. Lu, J. C. Hong, Y. C. Huang, K. H. Huang, S. Y. Chien, C. P. Chen and Y. J. Cheng, Fluorinated and methylated ortho-benzodipyrrole-based acceptors suppressing charge recombination and minimizing energy loss in organic photovoltaics, *Chem Sci*, 2025, **16**, 3259-3274.
28. X. He, F. Qi, X. Zou, Y. Li, H. Liu, X. Lu, K. S. Wong, A. K. Jen and W. C. H. Choy, Selenium substitution for dielectric constant improvement and hole-transfer acceleration in non-fullerene organic solar cells, *Nat. Commun.*, 2024, **15**, 2103.
29. S. Li, L. Zhan, N. Yao, X. Xia, Z. Chen, W. Yang, C. He, L. Zuo, M. Shi, H. Zhu, X. Lu, F. Zhang and H. Chen, Unveiling structure-performance relationships from multi-scales in non-fullerene organic photovoltaics, *Nat. Commun.*, 2021, **12**, 4627.
30. C. Yang, Q. An, H. R. Bai, H. F. Zhi, H. S. Ryu, A. Mahmood, X. Zhao, S. Zhang, H. Y. Woo and J. L. Wang, A Synergistic Strategy of Manipulating the Number of Selenophene Units and Dissymmetric Central Core of Small Molecular Acceptors Enables Polymer Solar Cells with 17.5 % Efficiency, *Angew. Chem. Int. Ed. Engl.*, 2021, **60**, 19241-19252.
31. W. Gao, B. Fan, F. Qi, F. Lin, R. Sun, X. Xia, J. Gao, C. Zhong, X. Lu, J. Min, F. Zhang, Z. Zhu, J. Luo and A. K. Y. Jen, Asymmetric Isomer Effects in Benzo[c][1,2,5]thiadiazole-Fused Nonacyclic Acceptors: Dielectric Constant and Molecular Crystallinity Control for Significant Photovoltaic Performance Enhancement, *Adv. Funct. Mater.*, 2021, **31**.
32. Y. Li, X. Huang, K. Ding, H. K. M. Sheriff, Jr., L. Ye, H. Liu, C. Z. Li, H. Ade and S. R. Forrest, Non-fullerene acceptor organic photovoltaics with intrinsic operational lifetimes over 30 years, *Nat. Commun.*, 2021, **12**, 5419.
33. X. Du, T. Heumueller, W. Gruber, A. Classen, T. Unruh, N. Li and C. J. Brabec, Efficient Polymer Solar Cells Based on Non-fullerene Acceptors with Potential Device Lifetime Approaching 10 Years, *Joule*, 2019, **3**, 215-226.
34. S. Li, Q. Fu, L. Meng, X. Wan, L. Ding, G. Lu, G. Lu, Z. Yao, C. Li and Y. Chen, Achieving over 18 % Efficiency Organic Solar Cell Enabled by a ZnO-Based Hybrid Electron Transport Layer with an Operational Lifetime up to 5 Years, *Angew. Chem. Int. Ed. Engl.*, 2022, **61**, e202207397.
35. H. Hou, W. Wang, Q. Kang, J. Wang, Z. Chen, Y. Wang, Y. Cui, Y. Yu, J. Zhu, H. Yan and J. Hou, Undoped MoOX with oxygen-rich vacancies as hole transport material for efficient indoor/outdoor organic solar cells, *Nano Energy*, 2024, **131**.
36. W. Sun, H. Chen, B. Zhang, Q. Cheng, H. Yang, Z. Chen, G. Zeng, J. Ding, W. Chen and Y. Li, Host-Guest Active Layer Enabling Annealing-Free, Nonhalogenated Green Solvent Processing for High-Performance Organic Solar Cells†, *Chin. J. Chem* . 2022, **40**, 2963-2972.
37. C. Zhang, M. Zhang, Q. Zhou, S. Chen, S. Kim, J. Yao, Z. Zhang, Y. Bai, Q. Chen, B. Chang, H. Fu, L. Xue, H. Wang, C. Yang and Z. G. Zhang, Diffusion-Limited Accepter Alloy Enables Highly Efficient and Stable Organic Solar Cells, *Adv. Funct. Mater.*, 2023, **33**.
38. J. W. Lee, C. Sun, H. Jeon, T. H. Q. Nguyen, T. N. L. Phan, X. Bao, Y. H. Kim and B. J. Kim,

Efficient and Photostable Organic Solar Cells Achieved by Alloyed Dimer Acceptors with Tailored Linker Structures, *Adv. Funct. Mater.*, 2024, **34**.

39. X. Yang, Y. Gao, L.-Y. Xu, X. Wu, X. Chen, Y. Shao, B. Xiao, S. Liu, J. Xia, R. Sun and J. Min, Efficient and stable all-small-molecule solar cells enabled by incorporating a designed giant molecule acceptor, *Energy Environ. Sci.*, 2024, **17**, 5962-5971.
40. J. Wan, T. Wang, R. Sun, X. Wu, S. Wang, M. Zhang and J. Min, Enabling Highly Efficient and Thermal-Stable Polymer Solar Cells through Semi-Alloy Acceptors Composed of a Hinge-Like Dimer: A Versatile Doping Protocol, *Adv. Mater.*, 2023, **35**, e2302592.
41. S. Kato, T. Furuya, A. Kobayashi, M. Nitani, Y. Ie, Y. Aso, T. Yoshihara, S. Tobita and Y. Nakamura, pi-Extended thiadiazoles fused with thienopyrrole or indole moieties: synthesis, structures, and properties, *J. Org. Chem.*, 2012, **77**, 7595-7606.
42. G. Kupgan, X. K. Chen and J. L. Brédas, Molecular packing of non-fullerene acceptors for organic solar cells: Distinctive local morphology in Y6 vs. ITIC derivatives, *Mater. Today Adv.*, 2021, **11**.
43. R. Po, G. Bianchi, C. Carbonera and A. Pellegrino, "All That Glisters Is Not Gold": An Analysis of the Synthetic Complexity of Efficient Polymer Donors for Polymer Solar Cells, *Macromolecules*, 2015, **48**, 453-461.
44. D. Luo, C. J. Brabec and A. K. K. Kyaw, Non-fused ring electron acceptors for high-performance and low-cost organic solar cells: Structure-function, stability and synthesis complexity analysis, *Nano Energy*, 2023, **114**.
45. A. K. K. Kyaw, D. H. Wang, C. Luo, Y. Cao, T. Q. Nguyen, G. C. Bazan and A. J. Heeger, Effects of Solvent Additives on Morphology, Charge Generation, Transport, and Recombination in Solution-Processed Small-Molecule Solar Cells, *Adv. Energy Mater.*, 2014, **4**.
46. P. Hartnagel and T. Kirchartz, Understanding the Light-Intensity Dependence of the Short-Circuit Current of Organic Solar Cells, *Adv. Theory Simul.*, 2020, **3**.
47. F. Gao, Z. Li, J. Wang, A. Rao, I. A. Howard, A. Abrusci, S. Massip, C. R. McNeill and N. C. Greenham, Trap-induced losses in hybrid photovoltaics, *Acs Nano*, 2014, **8**, 3213-3221.
48. V. D. Mihailetchi, J. Wildeman and P. W. Blom, Space-charge limited photocurrent, *Phys. Rev. Lett.*, 2005, **94**, 126602.
49. S. Oh, D. Jeong, K. Bae, G. U. Kim, T. N. L. Phan, J. W. Lee, J. Park, D. Lee, S. Cho and B. J. Kim, Impact of Linker Engineering in Core-Linked Dimeric Acceptors for High-Performance Organic Solar Cells, *Adv. Funct. Mater.*, 2024, **34**.
50. J. Wan, L. Zhang, Q. He, S. Liu, B. Huang, L. Hu, W. Zhou and Y. Chen, High-Performance Pseudoplanar Heterojunction Ternary Organic Solar Cells with Nonfullerene Alloyed Acceptor, *Adv. Funct. Mater.*, 2020, **30**.
51. J. Ren, S. Zhang, Z. Chen, T. Zhang, J. Qiao, J. Wang, L. Ma, Y. Xiao, Z. Li, J. Wang, X. Hao and J. Hou, Optimizing Molecular Packing via Steric Hindrance for Reducing Non-Radiative

Recombination in Organic Solar Cells, *Angew. Chem. Int. Ed. Engl.*, 2024, **63**, e202406153.

52. R. Wang, C. Zhang, Q. Li, Z. Zhang, X. Wang and M. Xiao, Charge Separation from an Intra-Moiety Intermediate State in the High-Performance PM6:Y6 Organic Photovoltaic Blend, *J. Am. Chem. Soc.*, 2020, **142**, 12751-12759.
53. C. M. Hung, C. J. Chih, K. H. Huang, Y. J. Xue, H. C. Chu, C. C. Tseng, C. H. Li, J. Y. Chen, B. H. Chen, S. D. Yang, Y. J. Cheng and P. T. Chou, Perovskite-Coupled NIR Organic Hybrid Solar Cells Achieving an 84.2% Fill Factor and a 25.2% Efficiency: A Comprehensive Mechanistic Exploration, *Angew. Chem. Int. Ed. Engl.*, 2025, **64**, e202501375.
54. C. M. Hung, S. F. Wang, W. C. Chao, J. L. Li, B. H. Chen, C. H. Lu, K. Y. Tu, S. D. Yang, W. Y. Hung, Y. Chi and P. T. Chou, High-performance near-infrared OLEDs maximized at 925 nm and 1022 nm through interfacial energy transfer, *Nat. Commun.*, 2024, **15**, 4664.
55. J. Wang, M. Zhang, J. Lin, Z. Zheng, L. Zhu, P. Bi, H. Liang, X. Guo, J. Wu, Y. Wang, L. Yu, J. Li, J. Lv, X. Liu, F. Liu, J. Hou and Y. Li, An asymmetric wide-bandgap acceptor simultaneously enabling highly efficient single-junction and tandem organic solar cells, *Energy Environ. Sci.*, 2022, **15**, 1585-1593.
56. Y. Xu, H. Yao, L. Ma, J. Wang and J. Hou, Efficient charge generation at low energy losses in organic solar cells: a key issues review, *Rep. Prog. Phys.*, 2020, **83**, 082601.
57. O. D. Miller, E. Yablonovitch and S. R. Kurtz, Strong Internal and External Luminescence as Solar Cells Approach the Shockley–Queisser Limit, *IEEE J. Photovolt.*, 2012, **2**, 303-311.
58. K. Vandewal, K. Tvingstedt, A. Gadisa, O. Inganäs and J. V. Manca, Relating the open-circuit voltage to interface molecular properties of donor:acceptor bulk heterojunction solar cells, *Phys. Rev. B*, 2010, **81**.
59. P. Bi, C. An, T. Zhang, Z. Chen, Y. Xu, Y. Cui, J. Wang, J. Li, Y. Wang, J. Ren, X. Hao, S. Zhang and J. Hou, Achieving 31% efficiency in organic photovoltaic cells under indoor light using a low energetic disorder polymer donor, *J. Mater. Chem. A*, 2023, **11**, 983-991.
60. X.-K. Chen, D. Qian, Y. Wang, T. Kirchartz, W. Tress, H. Yao, J. Yuan, M. Hülsbeck, M. Zhang, Y. Zou, Y. Sun, Y. Li, J. Hou, O. Inganäs, V. Coropceanu, J.-L. Bredas and F. Gao, A unified description of non-radiative voltage losses in organic solar cells, *Nat. Energy*, 2021, **6**, 799-806.
61. F. D. Eisner, M. Azzouzi, Z. Fei, X. Hou, T. D. Anthopoulos, T. J. S. Dennis, M. Heeney and J. Nelson, Hybridization of Local Exciton and Charge-Transfer States Reduces Nonradiative Voltage Losses in Organic Solar Cells, *J. Am. Chem. Soc.*, 2019, **141**, 6362-6374.
62. H. Choi, S. U. Ryu, D. H. Lee, H. Kim, S. Song, H. I. Kim and T. Park, Advancements in Organic-Based Hybrid Tandem Solar Cells Considering Light Absorption and Spectral Matching of Organic Materials, *ACS Energy Lett.*, 2024, **9**, 3136-3168.
63. S. M. Pratik, G. Kupgan, J.-L. Brédas and V. Coropceanu, Analysis of the charge generation and recombination processes in the PM6:Y6 organic solar cell, *Energy Environ. Sci.*, 2025, **18**, 841-852.

64. D. He, F. Zhao, C. Wang and Y. Lin, Non-Radiative Recombination Energy Losses in Non-Fullerene Organic Solar Cells, *Adv. Funct. Mater.*, 2022, **32**.
65. O. V. Mikhnenko, P. W. M. Blom and T.-Q. Nguyen, Exciton diffusion in organic semiconductors, *Energy Environ. Sci.*, 2015, **8**, 1867-1888.
66. F. Urbach, The Long-Wavelength Edge of Photographic Sensitivity and of the Electronic Absorption of Solids, *Phys. Rev.*, 1953, **92**, 1324-1324.
67. J.-W. Lee, J. Kim, T. H.-Q. Nguyen, D. C. Lee, Z. Tan, J. Park, T. N.-L. Phan, S. Cho and B. J. Kim, High efficiency and thermally stable ternary all-polymer solar cells achieved by alloyed vinyl-linked polymerized small-molecule acceptors, *Nano Energy*, 2024, **122**.
68. J. W. Lee, J. S. Park, H. Jeon, S. Lee, D. Jeong, C. Lee, Y. H. Kim and B. J. Kim, Recent progress and prospects of dimer and multimer acceptors for efficient and stable polymer solar cells, *Chem. Soc. Rev.*, 2024, **53**, 4674-4706.
69. C.-C. Tseng, L.-L. Yeh, C.-Y. Chang, C.-L. Huang, C.-L. Tsai, Y.-J. Xue, F.-C. Chen, C.-S. Hsu, T.-Y. Chu, J. Lu, U. S. Jeng and Y.-J. Cheng, A C6F5-functionalized benzimidazole acceptor enabling supramolecular fluorinated interactions for enhanced photovoltaic performance and thermal stability, *J. Mater. Chem. A*, 2025, DOI: 10.1039/d5ta02405f.
70. Y. Choi, D. Kim, S. U. Ryu, H. Kim, S. Kim, M. Kim and T. Park, Stability of Organic Photovoltaics: From Root Causes to Advanced Analytical Techniques, *Adv. Energy Mater.*, 2025, DOI: 10.1002/aenm.202501340.
71. Z. Wang, Y. Guo, X. Liu, W. Shu, G. Han, K. Ding, S. Mukherjee, N. Zhang, H. L. Yip, Y. Yi, H. Ade and P. C. Y. Chow, The role of interfacial donor-acceptor percolation in efficient and stable all-polymer solar cells, *Nat. Commun.*, 2024, **15**, 1212.

DOI: 10.1039/D5SC04976H

Effect of Halogen/Chalcogen Substitution on the Dielectric Constant of Asymmetric Acceptor Alloys to Improve the Efficiency and Stability of Inverted Organic Photovoltaics

Yan-Bo Wang, Yung-Jing Xue, Chieh-Ming Hung, Kuo-Hsiu Huang, Bing-Huang Jiang, Chia-Lin Tsai, Yu-Chi Huang, Hong-Yi Chen, Shang-Da Yang, Su-Ying Chien, Chih-Ping Chen, Pi-Tai Chou and Yen-Ju Cheng**

Data Availability Statement:

The data that supports the findings of this study are available in the manuscript and Supporting Information of this article. The X-ray crystallographic coordinates for structures of CBr_2B, CBrB and CBrB-Cl have been deposited at the Cambridge Crystallographic Data Centre (CCDC) with CCDC number 2452218, 2452219 and 2452220.